Interferometric Synthetic Aperture Radar Statistical Inference in Deformation Measurement and Geophysical Inversion

A review

CHISHENG WANG, LING CHANG, XIANG-SHENG WANG, BOCHEN ZHANG, AND ALFRED STEIN

With the rapid advancements in synthetic aperture radar (SAR) satellites and associated processing algorithms over recent decades, interferometric SAR (InSAR) has emerged as a routine method for monitoring large-scale ground deformation and interpreting geophysical

Digital Object Identifier 10.1109/MGRS.2023.3344159
Date of current version: 2 January 2024

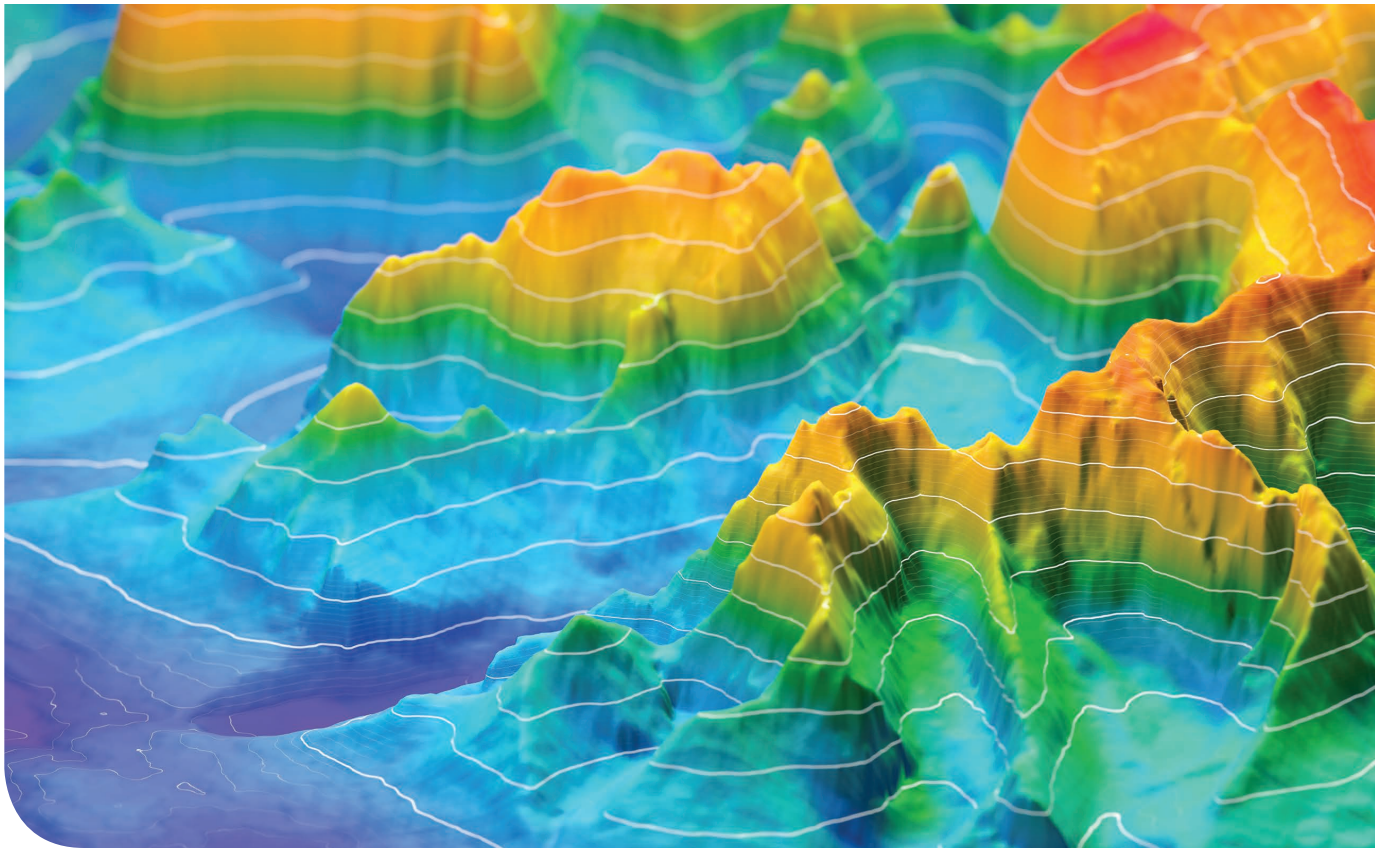

2473-2397/24©2024IEEE

Authorized licensed use limited to: Shaanxi Normal University. Downloaded on March 14,2024 at 04:23:51 UTC from IEEE Xplore. Restrictions apply.

processes. Statistical inference serves as a major component in InSAR technique developments and applications. This article provides an overview of InSAR deformation measurement and InSAR-constrained geophysical inversion, using a statistical inference point of view. Its objectives are to facilitate understanding of the method by addressing its underlying mathematical challenges. We begin by introducing the concept of statistical inference and the structure of our content organization framework. Next, we investigate the distinct concerns associated with statistical inference in InSAR deformation measurement and InSAR-constrained geophysical inversion. Finally, we propose several significant directions for future research. Table 1 includes abbreviations used throughout this article. Additionally, we highlight relevant resources, such as mathematical background, open source codes, and data repositories, in an appendix, which is available as supplementary material at https://doi.org/10.1109/MGRS.2023.3344159.

MOTIVATION

In recent decades, InSAR has emerged to be a powerful method for measuring ground deformation and studying geophysical processes [1], [2], [3]. InSAR measurements, with millimeter precision and large coverage areas, enable the study of various geophysical phenomena. Using InSAR, researchers can, for instance, monitor ice stream movement [4], measure fault shifting during earthquakes [5], and observe ground changes resulting from fluid injection or extraction [6].

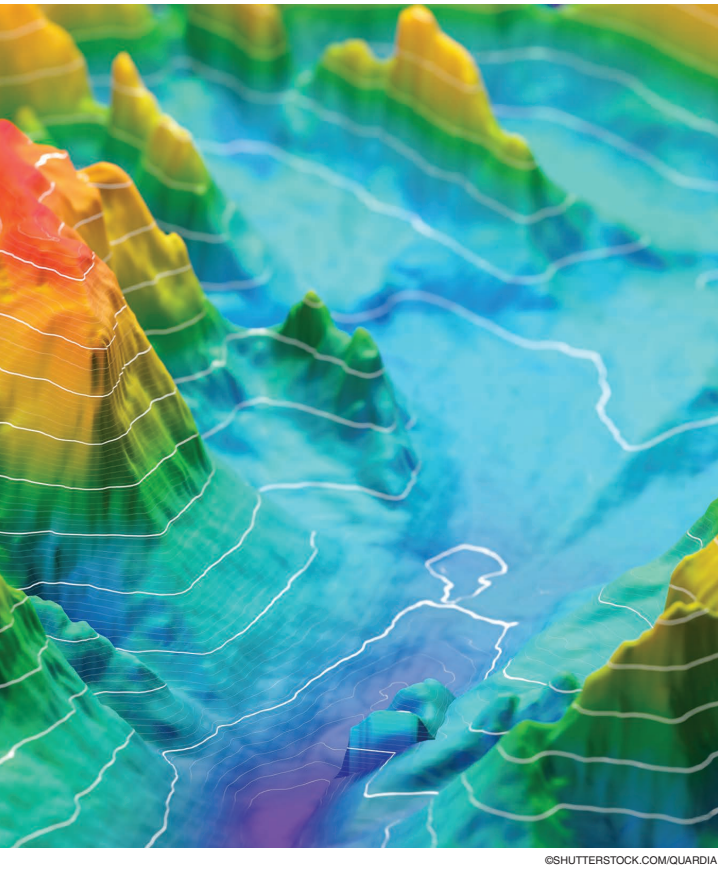

©SHUTTERSTOCK.COM/QUARDIA

TABLE 1. ABBREIVATIONS USED IN THIS ARTICLE.

ABBREVIATION	FULL NAME
CCG	Complex circular gaussian
MLE	Maximum likelihood estimation
pdf	Probability density function
CRLB	Cramer–Rao lower bound
SCM	Sample coherence matrix
EP	Error propagation
CI	Credible interval
InSAR	Interferometric synthetic aperture radar
SLC	Single-look complex
i.i.d.	Independent identically distributed
DS	Distributed scatterer
DSI	DS interferometry
SBAS	Small baseline subset
TomoSAR	Tomographic SAR
PS	Persistent scatterer
PSI	PS interferometry
BIC	Bayesian information criterion
FIM	Fisher information matrix
MCMC	Markov chain Monte Carlo
D-TomoSAR	Differential TomoSAR
APS	Atmospheric phase screen

InSAR studies in geophysics typically consist of two stages: first, processing SAR images to produce InSAR deformation measurements and second, inverting these measurements to derive geophysical parameters. Over time, numerous advanced methods have emerged in this domain [7], [8], [9], [10]. While these methods are developed by various scientific communities, the fundamental mathematical issues they address are universally connected to statistical inference. Both InSAR deformation measurement, which estimates displacement parameters from SAR data, and geophysical inversion, which estimates geophysical parameters from displacement measurements, tackle similar statistical inference challenges. These challenges include constructing a proper statistical model, addressing ill-posed estimation issues, selecting multiple alternative models, and evaluating the quality of the estimated parameters.

The diverse backgrounds of researchers involved in method development, including fields like electrical engineering, geodesy, remote sensing, and computer science, have led to state-of-the-art methods being described using varied terminologies. The complexity of these terminologies often makes them challenging to understand. Nonetheless, comprehending the fundamentals of InSAR processing and geophysical inversion is crucial for researchers. This importance is underscored by the frequent need for manual intervention in achieving optimal results, given the intricate nature of application scenarios and imperfections in SAR data. A robust grasp of the core mathematical concepts can provide deeper insights. Notably, no existing work has yet to describe these

Authorized licensed use limited to: Shaanxi Normal University. Downloaded on March 14,2024 at 04:23:51 UTC from IEEE Xplore. Restrictions apply.

methods by specifically addressing their shared mathematical challenges. Our goal is to bridge this gap by offering a concise summary of current knowledge of InSAR deformation measurement and InSAR-constrained geophysical inversion methods, with a focus on statistical inference.

INTRODUCTION TO RELEVANT STATISTICAL INFERENCE CONCEPTS

Statistical inference is defined as the process of learning characteristics of a population from a sample. Basic concepts in statistical inference include statistical modeling, point estimation, interval estimation, and hypothesis testing [11]. A statistical model describes the complex phenomena that generate the data. It typically consists of mathematical formulations that link parameters and observations and assumptions about the probability distribution of the observed variables. After selecting a statistical model, we can deduce statistical propositions using point estimation, interval estimation, and hypothesis testing. Specifically, point estimation gives a single most likely value for a parameter, while interval estimation provides a range where the parameter value is expected to fall with a specific degree of confidence. Hypothesis testing decides whether the data at hand sufficiently support a particular hypothesis.

InSAR deformation measurement and InSAR-constrained geophysical inversion are typical examples of statistical inference, using the observed data to derive estimates and test hypotheses. Their statistical inferences can be generally divided into three stages (Figure 1):

1) *Pre-estimation*: A statistical model is constructed for the parameter estimation problem. It is defined by the observation variables, parameter variables, and probability function.
2) *Estimation*: Typically, either maximum likelihood estimation (MLE) or Bayesian estimation is selected based on the inclusion of any a priori knowledge. An optimization algorithm is then employed to search for the solution based on the criterion defined by the estimator;
3) *Postestimation*: If alternative function models are considered, model testing/selection based upon hypothesis testing or information criteria is also required. Meanwhile, the quality of the parameter estimation can also be assessed using different approaches, such as the Cramer–Rao lower bound (CRLB), error propagation (EP), or the credible interval (CI).

In this article, mathematical symbols maintain distinct meanings within their respective sections. For example, symbols in the "Statistical Inference in Interferometric Synthetic Aperture Radar Deformation Measurement" section have definitions specific to that context, while those in the "Statistical Inference in Interferometric Synthetic Aperture Radar-Constrained Geophysical Inversion" section pertain only to that section.

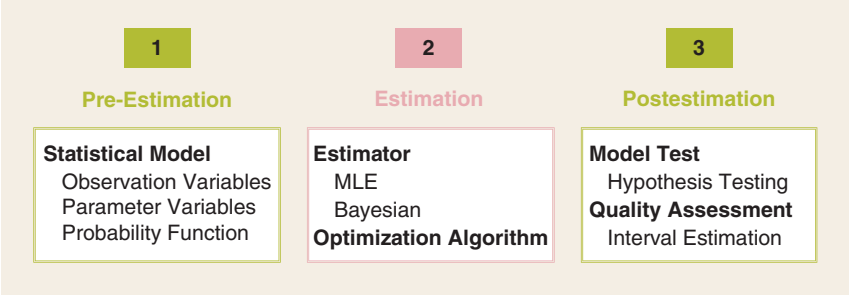

FIGURE 1. The main stages for conducting statistical inference. MLE: maximum likelihood estimation.

STATISTICAL INFERENCE IN INTERFEROMETRIC SYNTHETIC APERTURE RADAR DEFORMATION MEASUREMENT

InSAR processing is a remote sensing method that aims to extract Earth surface deformation parameters from initial single-look complex (SLC) data. It uses different statistical models and estimators to accommodate variations in application scenarios and scatterers.

PROBLEM DEFINITION

TYPES OF SCATTERERS

SLC observations from SAR images are represented as complex numbers. Such a complex number consists of the cumulative reflection of all the subresolution scatterers

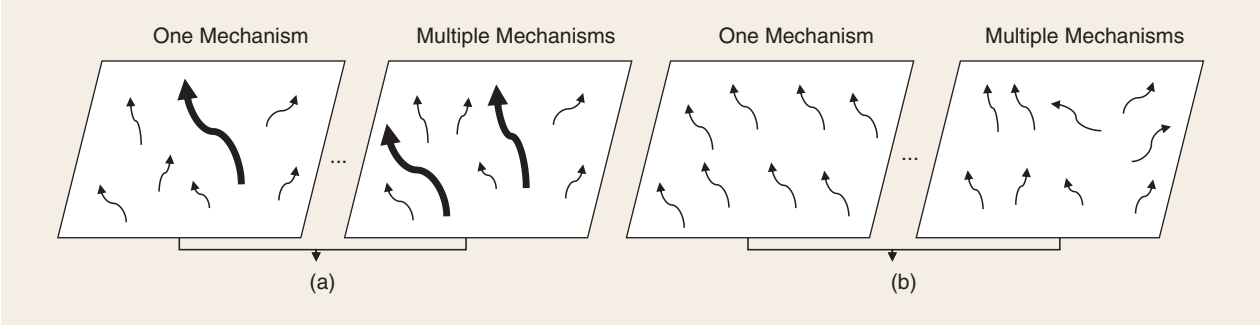

FIGURE 2. The primary types of SAR scatterers: (a) PSs and (b) DSs.

Authorized licensed use limited to: Shaanxi Normal University. Downloaded on March 14,2024 at 04:23:51 UTC from IEEE Xplore. Restrictions apply.

within a resolution cell. According to the behavior of subresolution scatterers, the radar pixel can be classified into two categories: persistent scatterers (PSs) and distributed scatterers (DSs). PSs are stable radar-reflective points providing consistent backscattering characteristics over time. DSs, in contrast, are more widespread radar reflections from various spatially distributed objects or surfaces, resulting in less stable backscattering behavior over time. Additionally, PSs and DSs are further divided into subcategories according to the number of mechanisms inside the pixel, i.e., single-mechanism PS, multimechanism PS, single-mechanism DS and multimechanism DS (Figure 2). The statistical model and estimation approach vary for different types of scatterers, as detailed in the subsequent text.

MAIN PROCESSING CHAIN

The primary categories within multitemporal InSAR (MT-InSAR), including PS interferometry (PSI), DS interferometry (DSI), the small baseline subset (SBAS), differential tomographic SAR (D-TomoSAR), and so on [7], [8], were conceived independently by various inventors at different times. This has led to inconsistencies in their naming conventions, as also pointed out by Hopper et al. [8]. Moreover, the boundaries among these methods are not strictly defined, especially since certain processing steps can overlap across categories. This review aims to describe the statistical inference problems related to InSAR. Consequently, our content is organized around the specific parameter estimation problems encountered, rather than strictly adhering to conventional methodological categories.

InSAR deformation measurement involves using SAR image observations as input, which then leads to the generation of deformation results as output. This might seem like a straightforward parameter estimation process that uses SAR SLC observation to determine the deformation parameters. However, due to the complexity of scatterer types and varying application scenarios, there are multiple strategies and substeps involved (Figure 3). Specifically, for single-mechanism scatterers, this process is primarily divided into three steps: wrapped phase estimation, unwrapped phase estimation, and deformation estimation. For multiple-mechanism scatterers, processing strategies vary depending on the application scenarios and types of scatterers. A common application scenario involves estimating the height and deformation for each mechanism through a D-TomoSAR step.

WRAPPED PHASE ESTIMATION

The initial step in InSAR deformation measurement involves transitioning from SAR data to a wrapped interferometric phase. In this context, the observed variable is the SAR SLC data, while the parameter variable pertains to the interferometric phase. Typically, as each pixel has only one observation in each SLC image, there is no redundancy in observations. Computationally, this step should be straightforward, eliminating the need for statistical methods in parameter estimation. In fact, for PS points, this phase is merely a complex conjugate multiplication calculation, aligning with the PSI processing method. However, for DSs, the phase derived directly from a single pixel exhibits high variance, making it challenging for subsequent processing. To enhance phase quality in SAR observations, we often assume that the observations are spatially stationary and ergodic. By doing so, we can treat observations from neighboring pixels as repeated measurements, which allows us to refine the interferometric phase estimation. Both DSI and the SBAS employ this concept at this stage. This procedure is commonly termed *filtering*.

PRE-ESTIMATION: STATISTICAL MODEL

The complex value observation (z) on a DS is composed of many small reflections. If subresolution weak scatterers share the same scattering mechanism, their summary

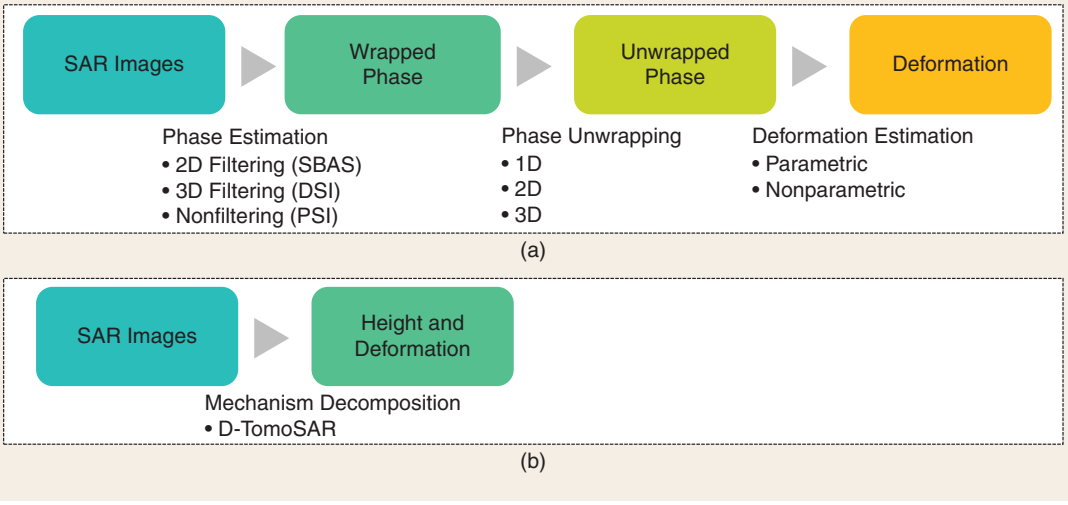

FIGURE 3. Various strategies and substeps used in InSAR deformation measurement: (a) one mechanism and (b) multiple mechanisms.

Authorized licensed use limited to: Shaanxi Normal University. Downloaded on March 14,2024 at 04:23:51 UTC from IEEE Xplore. Restrictions apply.

follows a complex circular Gaussian (CCG) distribution by applying the central limit theorem:

$$\begin{gathered} z = x_s + iy_s \\ \text{with } x_s, y_s \sim N(0, \sigma_z^2) \\ \text{and } z \sim NC(0, 2\sigma_z^2) \end{gathered} \tag{1}$$

where $x_s \in \mathbb{R}$ is the real part of the complex value observation z, $y_s \in \mathbb{R}$ is the imagery part of the complex value observation z, and $\sigma_z^2 \in \mathbb{R}$ is the variance of x_s and y_s.

Including the temporal dimension, the 1D SLC observation z is extended to p-dimensional observation vector $\boldsymbol{z}$. The observations then follow a p-variate CCG distribution:

$$\boldsymbol{z} \sim NC(0, \boldsymbol{\Gamma}) \tag{2}$$

where $p \in \mathbb{N}$ is the number of SLC images, $\boldsymbol{z} \in \mathbb{C}^{p\times 1}$ is the random SLC observation vector along time for a pixel, and $\boldsymbol{\Gamma} \in \mathbb{C}^{p\times p}$ is the coherence matrix of $\boldsymbol{z}$.

Under the one-scattering-mechanism assumption, the complex coherence matrix $\boldsymbol{\Gamma} \in \mathbb{C}^{p\times p}$ can be decomposed into a real-value coherence matrix and a diagonal complex matrix with consistent phase series:

$$\boldsymbol{\Gamma} = \boldsymbol{\Theta} \boldsymbol{G} \boldsymbol{\Theta}^H \tag{3}$$

where $\boldsymbol{G} \in \mathbb{R}^{p\times p}$ is the real-value coherence matrix of the interferograms for a pixel, $\boldsymbol{\theta} \in \mathbb{R}^{p\times 1}$ is the consistent phase series for a pixel, and $\boldsymbol{\Theta} \in \mathbb{C}^{p\times p}$ is the complex matrix containing the consistent phase series $\boldsymbol{\theta}$, with $\boldsymbol{\Theta} = \text{diag}(e^{i\boldsymbol{\theta}})$.

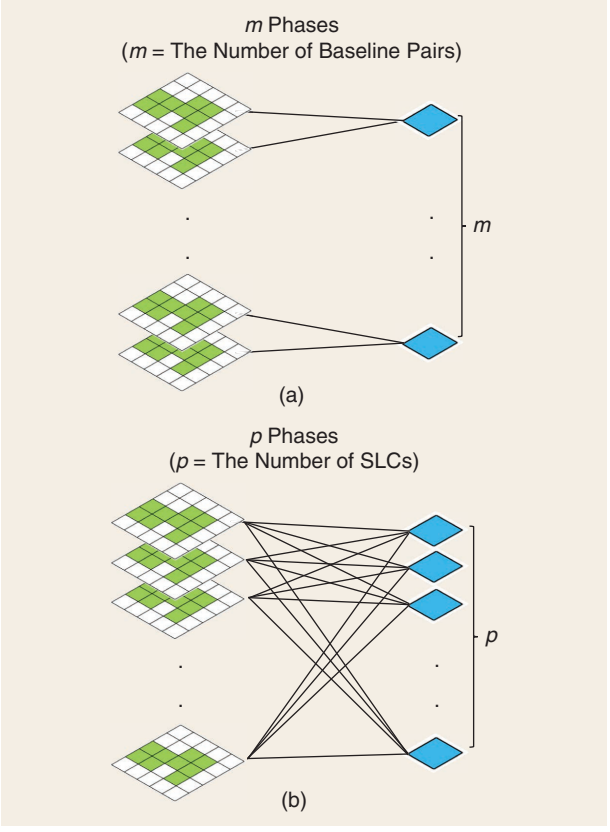

FIGURE 4. The phase estimation in (a) the SBAS and (b) DSI.

By the way, the stochastic characteristics of PSs are often considered a deterministic signal plus random noise, unlike DSs, which lack a deterministic signal [12]. This random noise can also be considered to follow a CCG distribution. In actual processing, the temporal random characteristics of these noises are usually simplified as independent identically distributed (i.i.d.). Since PSs are not addressed in this step, their stochastic characteristics will be discussed in greater detail in subsequent sections.

Let us assume a real-value coherence matrix and consistent phase series to be the parameters. The conditional probability density function (pdf) of the time series data vector $\boldsymbol{z}$ can be given [13], [14], [15]:

$$f(\boldsymbol{z}|\boldsymbol{G}, \boldsymbol{\theta}) = \pi^{-p} (\det[\boldsymbol{G}])^{-1} \exp(-\boldsymbol{z}^H \boldsymbol{\Theta} \boldsymbol{G}^{-1} \boldsymbol{\Theta}^H \boldsymbol{z})) \tag{4}$$

where det is the determinant operator and $f(\,.\,)$ is the probability function.

Note that determining the absolute phase series for each SLC image is ambiguous. In the time series, the phase of a chosen image is designated as zero, and the remaining phases are measured relative to this chosen datum [16]. Therefore, the estimated parameters $\boldsymbol{\Theta}$ are equivalent to the interferometric phase, with this arbitrary datum as the master image. Additionally, $\boldsymbol{G}$ here is a parameter variable. In the earliest DSI methods, the SCM was used as a substitute, turning this parameter variable into a known variable. However, in such a processing approach, the estimation bias of the SCM has a significant impact on the phase estimation. Some recent works in the literature have discussed this issue [13], [17].

In summary, the statistical model for wrapped phase estimation is given by

$$\begin{gathered} \text{Observation variable: } \boldsymbol{z} \\ \text{Parameter variables: } \boldsymbol{G}, \boldsymbol{\theta} \\ \text{pdf: } f(\boldsymbol{z}|\boldsymbol{G}, \boldsymbol{\theta}) \text{ in formula (4).} \end{gathered} \tag{5}$$

PARAMETER ESTIMATION

Both DSI and the SBAS estimate the phase based on the statistical model in formula (5), that is, estimating parameter $\boldsymbol{\Theta}$ through observation $\boldsymbol{z}$. However, their strategies differ. The SBAS estimates each interferometric pair separately, while DSI estimates the entire time series at once (Figure 4). As a result, the wrapped phase estimation in the SBAS can be considered 2D spatial filtering (without using the temporal dimension constraint), leading to phases of interferometric pairs that are inconsistent over the time series. On the other hand, DSI can be seen as 3D spatiotemporal filtering, producing phases that are consistent over time and share the same characteristics as the interferometric phases of PSI. After the DSI wrapped phase estimation, DSs can be processed in subsequent steps in the same manner as PSs.

In the SBAS, phase estimation is performed on a series of small baseline interferograms, with each interferogram

Authorized licensed use limited to: Shaanxi Normal University. Downloaded on March 14,2024 at 04:23:51 UTC from IEEE Xplore. Restrictions apply.

estimated once. Consequently, the statistical model in formula (5) simplifies to a special case where $p = 2$. This becomes equivalent to the maximum likelihood estimate of the interferogram phase between the ith and jth SLC, which is determined by [18], [19]

$$\hat{\phi}_{i,j} = \angle \sum_{k=1}^{N} z_{i,k} z^{H}{}_{j,k} \tag{6}$$

where $N \in \mathbb{N}$ is the number of adjacent pixels in the homogeneous patch, $\hat{}$: is the estimation of a variable, $\phi_{i,j} \in \mathbb{R}$ is the interferometric phase between the ith and jth SLC, and $z_{i,k} \in \mathbb{R}$ is the SLC observation for pixel k in the ith SLC.

When the samples originate from a rectangular area adjacent to the pixel, it is equal to using a multilook filter. This process employs a basic rectangular neighborhood window for averaging, commonly referred to as a *boxcar filter*. Despite suffering from issues such as decreased resolution and invalid assumptions due to oversimplified processing, it is still widely utilized, particularly in large-scale scenes, due to its ease of implementation. In response, many adaptive filters have been developed to address the resolution reduction and independent identical distribution assumption issues caused by simple multilook filtering. These methods can be roughly divided into four categories: spatial-domain Bayesian methods (such as Lee filtering [20] and improved Lee filtering [21]), transform-domain Bayesian methods (such as the Goldstein filter [22] and wavelet filter [23]), selection-based filters (such as nonlocal filters [24]), and sparse constraint-based filters [25]. Additionally, there has been an effort to incorporate temporal information to enhance 2D filtering in the SBAS [26]. Recently, deep neural networks have also shown great potential for SAR image filtering [27].

In DSI, p is exactly the number of SLC images. Under the single-mechanism assumption, theoretically, MLE is the best estimation method. If $\boldsymbol{G}$ is assumed to be known and presented by the SCM, the MLE of the phase is given by [14], [15]

$$\hat{\theta} = \operatorname{argmax}\left\{ (e^{i\theta})^{H} (-|\hat{\boldsymbol{\Gamma}}|^{-1} \circ \hat{\boldsymbol{\Gamma}}) e^{j\theta} \right\} \tag{7}$$

where $\hat{\boldsymbol{\Gamma}}$ is the SCM, given by:

$$\hat{\boldsymbol{\Gamma}} = \frac{1}{N} \sum_{z \in \Omega} z z^{H} \tag{8}$$

where Ω is a homogeneous patch containing adjacent pixels.

If the SCM $\hat{\boldsymbol{\Gamma}}$ is not positive definite, additional modifications to the SCM may be necessary, such as inserting a damping factor [28] or incorporating calibration parameters [16], [29]. However, as the SCM is not the actual coherence matrix, any bias in the SCM can be propagated to the estimated parameters [30]. Recent efforts have been directed toward simultaneously resolving the coherence matrix and consistent phase series [13], [31], [32], which results in a new likelihood function, such as

$$\hat{\theta} = \operatorname{argmax}\{-\det(\operatorname{Re}[\boldsymbol{\Theta}^{H} \hat{\boldsymbol{\Gamma}} \boldsymbol{\Theta}])\} \tag{9}$$

where Re is the real part operator of complex values.

An example of DS phase estimation can be seen in Figure 5. After the wrapped phase estimation, the noise is significantly reduced compared to the original interferogram phase. It is worth noting that the MLE described above is based on the idea of a single scattering mechanism within the DS unit. Nonetheless, when there are multiple scattering mechanisms, the MLE can produce results that are

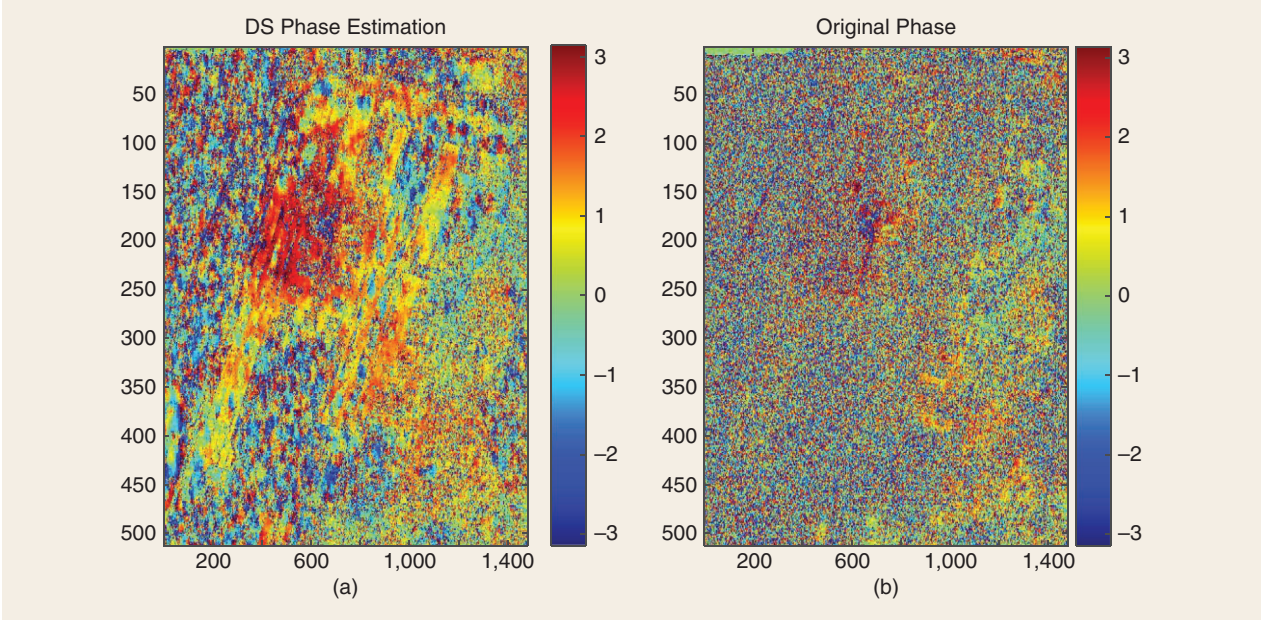

FIGURE 5. (a) DS interferometric phase estimation and (b) the original interferometric phase.

Authorized licensed use limited to: Shaanxi Normal University. Downloaded on March 14,2024 at 04:23:51 UTC from IEEE Xplore. Restrictions apply.

biased. Recent works in the literature have extensively examined this issue [33], [34], [35].

In addition to the direct MLE for the phase, several other techniques have been developed to either improve computational efficiency or address multiple scattering mechanisms. For instance, a sequential estimator was introduced to process large numbers of SAR images efficiently [36]. This is achieved by dividing the data stack into multiple mini-stacks, thereby avoiding the calculation of the full SCM. The Eigen-decomposition-based maximum likelihood estimator for interferometric phase (EMI) [16] was designed to utilize matrix decomposition in place of iterative problem solving, thus enhancing the algorithm's computational speed. Research indicates that when the height difference among the scattering center points related to different scattering mechanisms surpasses a certain threshold, their contributions can be considered approximately orthogonal. This insight allows the use of principal component analysis decomposition to segment the covariance matrix into several orthogonal components, facilitating the separation of distinct scattering mechanisms [37]. For a more in-depth discussion, readers can refer to references [38] and [39].

POSTESTIMATION

In general practice, this step does not involve model testing. After estimation, the main concern is the quality of the interferometric phase.

For the SBAS, the interferogram coherence can be used to represent the quality of the interferometric phase estimation. The relation between interferogram coherence and phase variance can be referenced in [12]. The interferogram coherence is given by

$$\gamma = \frac{E\{z_1 z_2^*\}}{\sqrt{E\{|z_1|^2\}E\{|z_2|^2\}}} = |\gamma| e^{j\phi_{1,2}} \tag{10}$$

where $\gamma \in \mathbb{R}$ is the interferogram coherence.

For DSI, the phase estimation is not derived from a direct mathematical formula but from the optimization of a nonlinear function. Its phase estimation quality can hardly be accurately quantified. Therefore, the CRLB is often used as an approximate representation. Specifically, the Fisher information matrix (FIM) associated with the consistent phase series reads

$$\boldsymbol{J} = 2N(\boldsymbol{\Gamma}^{-1} \circ \boldsymbol{\Gamma} - \boldsymbol{I}) \tag{11}$$

where $\circ$ is the Hadamard operation, referring to the element-by-element multiplication of two matrices; $\boldsymbol{J} \in \mathbb{C}^{p \times p}$ is the FIM; and $\boldsymbol{I}$ is the identity matrix.

The formula for the CRLB of consistent phase series is

$$\boldsymbol{\sigma}_{\theta}^2 = \mathrm{diag}\{(\boldsymbol{J}(m|m))^{-1}\}. \tag{12}$$

The operator $\mathrm{diag}\{\cdot\}$ retrieves the diagonal elements of a matrix; $\boldsymbol{J}(m|m)$ is obtained by removing the mth row and column of the matrix, where the index corresponds to the master scene. This removal results in $\boldsymbol{\sigma}_{\theta}^2$ containing the variance of $n-1$ estimated phases relative to the master scene. It is important to note that the phase variance of the master scene is zero and fixed as the datum of the time series, which means it is exempt from estimation. To say it differently, the mth phase is treated as a known random variable with the highest certainty and thus has zero variance.

However, it is evident that the calculation of the CRLB in DSI requires the value of coherence matrix $\boldsymbol{\Gamma}$, which is not available in real-world scenarios. As a result, the CRLB is often used in simulated experiments to evaluate the degree of approximation of the estimation method to the theoretical lower limit of accuracy.

In practice, ensemble coherence, which represents the degree of the phase residual after model fitting, is often taken for overall DSI quality assessment. The ensemble coherence is also named *posterior coherence* [13], [40] in some DSI studies. It can be expressed using the following formula:

$$\gamma_e = \frac{1}{K}\sum_{k=1}^{K} e^{jr_{\phi,k}} \tag{13}$$

where K is the number of residual phases, $r_{\phi,k} \in \mathbb{R}$ is the residual phase between the kth phase observation and the phase model, and $\gamma_e \in \mathbb{R}$ is the ensemble coherence.

UNWRAPPED PHASE ESTIMATION

After obtaining the wrapped phase, the next challenge is to estimate the unwrapped phase from it. This estimation problem is inherently underdetermined and requires additional assumptions. For time series InSAR, unwrapping methods can be broadly categorized into 1D (temporal) and 2D (spatial) phase unwrapping. In the case of PSI, a 1D approach is often employed [41], [42], where the phase observations for a specific pixel in the data stack are unwrapped over time. In the case of DSI, the interferometric phase of DSs is like that of PSs after the phase estimation step, and the subsequent processing method aligns with PSs, so the 1D approach is typically used also. In the case of the SBAS, a 2D approach is typically adopted, where the interferograms are unwrapped spatially. The 1D technique excels at accurately unwrapping phases in areas with discontinuities, though it demands a greater number of interferograms and insists on phase alignment with a set model. In contrast, the 2D approach can perform unwrapping with a reduced number of interferograms, offering enhanced adaptability in subsequent phase unwrapping stages. Yet, it may encounter unwrapping inaccuracies in regions where jumps disrupt the assumption of spatial continuity [7]. To fully leverage the 3D characteristics of signals, phase unwrapping methods in 3D space (azimuth, range, and time) have also been proposed [43], [44]. Phase unwrapping using machine learning has now become a new hotspot. A more comprehensive review of InSAR phase unwrapping can be found in [45] and [46]. Here, we use the 1D time unwrapping, which is frequently adopted in PSI, as an example to explain the estimation problem in unwrapping.

Authorized licensed use limited to: Shaanxi Normal University. Downloaded on March 14,2024 at 04:23:51 UTC from IEEE Xplore. Restrictions apply.

Phase unwrapping in the temporal dimension is an underdetermined problem, where many solutions exist. Here, we can assume that the wrapped phase series can be described by a phase model over time, and the range of the residual phase that is not described by the model is assumed to be $(-\pi, \pi]$. After estimating the parameters of the phase model, the problem of unwrapping in the time dimension is naturally solved. Therefore, the phase unwrapping problem becomes a problem of solving the phase model parameters over time.

However, it should be noted that 1D time unwrapping can sometimes introduce significant uncertainty when the data are not well described by the phase model. In practice, the unwrapping process is more complex, incorporating various strategies. Typically, parametric estimation derived from 1D time unwrapping is used as an initial approximation, which is subsequently refined using phase unwrapping algorithms that function in 2D [47] or 3D [48] spaces.

PRE-ESTIMATION: STATISTICAL MODEL

A PS observation is affected by various factors, such as atmospheric effects and topography. The PS interferometric phase observation equation is given by

$$\boldsymbol{\phi} = W(\boldsymbol{\phi}_D + \boldsymbol{\phi}_A + \boldsymbol{\phi}_O + \boldsymbol{\phi}_H + \boldsymbol{\phi}_N) \tag{14}$$

where $\boldsymbol{\phi}$ is the interferometric phase series, $\boldsymbol{\phi}_D$ is the deformation phase, $\boldsymbol{\phi}_A$ is the atmospheric phase, $\boldsymbol{\phi}_O$ is the orbital phase, $\boldsymbol{\phi}_H$ is the topographic phase, and $\boldsymbol{\phi}_N$ is random noise.

Among all the signal components in PSs, $\boldsymbol{\phi}_D$ and $\boldsymbol{\phi}_H$ can be represented by parameterized models. For example, $\boldsymbol{\phi}_D$ could be modeled using linear, exponential, periodic, or other deformation models with time as a variable, and $\boldsymbol{\phi}_H$ could be modeled by a linear function with the baseline as a variable. We simplify the phase observation as

$$\boldsymbol{\phi} = W(\Phi(\boldsymbol{m}) + \boldsymbol{\phi}_A + \boldsymbol{\phi}_O + \boldsymbol{\phi}_N) \tag{15}$$

where $\boldsymbol{m}$ is the vector of unknown parameters to be estimated and $\boldsymbol{\Phi}(\boldsymbol{m})$ is the phase model with parameters $\boldsymbol{m}$.

However, the atmospheric phase often also occupies a significant portion, making the estimation of model parameters challenging. A common method involves creating a "double-difference" phase by computing the phase differences between nearby candidate pixels [49], [50], [51]. The edge connecting two points is typically referred to as an *arc*:

$$\Delta\boldsymbol{\phi} = W(\boldsymbol{\Phi}(\Delta\boldsymbol{m}) + \Delta\boldsymbol{\phi}_A + \Delta\boldsymbol{\phi}_O + \Delta\boldsymbol{\phi}_N) \tag{16}$$

where Δ is a symbol representing the difference between two points on an arc.

We write the phase observation equation in the form of the complex domain:

$$\Delta\boldsymbol{g} = \boldsymbol{\Psi}(\Delta\boldsymbol{m}) + \boldsymbol{w}. \tag{17}$$

The arc complex interferogram observation $\Delta\boldsymbol{g}$ consists of the model arc component $\boldsymbol{\Psi}(\Delta\boldsymbol{m})$ and the unmodelled component $\boldsymbol{w}$. Commonly, the unmodeled part is primarily caused by atmospheric disturbances, orbital errors, and thermal noise, which are uncorrelated over time. Reflections from the DSs within the resolution grid can further contribute to the unmodeled values, and these are correlated over time. Since uncorrelated influences, such as atmospheric disturbances and thermal noise, make the primary contribution to the unmodeled part, the unmodeled values are often assumed to be zero-mean i.i.d. CCG noise with a variance of σ_w^2:

$$\boldsymbol{w} \sim NC(0, 2\sigma_w^2\boldsymbol{I}). \tag{18}$$

For a general function model $\Psi(\Delta\boldsymbol{m})$, the conditional pdf for a PS arc wrapped phase given the model parameters is

$$f(\Delta\boldsymbol{g}\,|\,\Delta\boldsymbol{m}) = (2\sigma_w^2\pi)^{-p} \exp\Big(-\frac{1}{2\sigma_w^2}(\Delta\boldsymbol{g} - \Psi(\Delta\boldsymbol{m}))^H(\Delta\boldsymbol{g} - \Psi(\Delta\boldsymbol{m}))\Big). \tag{19}$$

Note that the estimated parameters $\Delta\boldsymbol{m}$ on arcs can be integrated into parameters $\boldsymbol{m}$ on pixels through spatial network adjustment. Then, the time series unwrapped phase on pixels can be obtained.

In summary, the statistical model for the 1D unwrapped phase estimation problem is given by

$$\begin{gathered}\text{Observation variable: } \Delta\boldsymbol{g} \\ \text{Parameter variable: } \Delta\boldsymbol{m} \\ \text{pdf: } f(\Delta\boldsymbol{g}\,|\,\Delta\boldsymbol{m}) \text{ in formula (19).}\end{gathered} \tag{20}$$

PARAMETER ESTIMATION

The MLE is an appropriate estimator for solving the problem defined in formula (20). The MLE, obtained by maximizing the probability function $f(\Delta\boldsymbol{g}\,|\,\Delta\boldsymbol{m})$, is equivalent to maximizing the periodogram [28], [52]:

$$\widehat{\Delta\boldsymbol{m}} = \operatorname{argmax}\left\{\left|\frac{1}{p}\sum_{k=1}^{p}\Delta\boldsymbol{g}_k\boldsymbol{\Psi}_k^H(\Delta\boldsymbol{m})\right|\right\}. \tag{21}$$

Although the periodogram is a widely recognized method for parameter estimation in InSAR, few studies link it to the probability function. Nonetheless, it is crucial to highlight the statistical model underlying it. Given this context, some robust and advanced statistical models and estimation algorithms could potentially be applied.

Considering the elevation and deformation parameters, the phase series model takes the form of

$$\boldsymbol{\Psi}_k = \exp\left(j2\pi\left(\frac{\xi_k\Delta h}{\sin\theta} + \frac{2\Delta d(t_k)}{\lambda}\right)\right) \quad \text{with } \xi_k = \frac{-2b_k}{(\lambda r)} \tag{22}$$

where θ is the look angle, h is the height, t_k is the time variable for the kth SLC image, $d(t_k)$ is the displacement as a function of t_k, λ is the wavelength of the SAR system, and b_k is the orthogonal baseline between the kth SLC and master SLC.

Authorized licensed use limited to: Shaanxi Normal University. Downloaded on March 14,2024 at 04:23:51 UTC from IEEE Xplore. Restrictions apply.

The MLE of elevation and deformation parameters for PS points can be transformed into maximizing the periodogram:

$$\widehat{\Delta \boldsymbol{m}} = \operatorname{argmax}\left\{\left| \frac{1}{p}\sum_{k=1}^{p} \Delta g_k \exp\left(-j2\pi\left(\frac{\xi_k \Delta h}{\sin\theta} + \frac{2\Delta d(t_k)}{\lambda}\right)\right)\right|\right\}. \tag{23}$$

Here, the parameter vector $\Delta \boldsymbol{m}$ is composed of the elevation parameter Δh and the coefficients of the deformation function $\Delta d(t_k)$ on an arc. To obtain the corresponding parameter solutions, one can discretize the elevation residuals and deformation coefficients (e.g., velocity and thermal coefficient) and use a grid search approach (Figure 6).

POSTESTIMATION

Similar to the DSI wrapped phase estimation, the statistical model for 1D temporal unwrapping operates in the complex domain, and its estimation process is nonlinear. As a result, the CRLB used in DSI quality assessment can also be applied to approximate the variance of estimated parameters. However, few studies have tackled periodogram estimation in 1D temporal unwrapping from a statistical viewpoint, making this area relatively uncharted. Nonetheless, a related yet more general estimation problem was analyzed earlier [52]. Drawing from this research, Ferretti et al. derived an approximation of the variance for estimating height and velocity parameters using the periodogram in their groundbreaking work on PSI [42].

In practice, ensemble coherence is widely used to assess the quality of parameter estimation. It shares the same formula as DSI but is often termed *temporal coherence* [53]. This metric is also frequently used as a criterion for selecting high-quality arcs or pixels for subsequent processing.

DEFORMATION ESTIMATION

Once the unwrapped interferograms are obtained, the final step is to estimate the deformation. In this context, these unwrapped interferograms act as observations. The parameters are the deformation parameters. They can be either a series of deformations over time or a limited set of deformation parameters from a predefined deformation model.

For the SBAS and PSI/DSI, the types of unwrapped interferograms handled are different. The SBAS works with multimaster unwrapped interferograms, while PSI/DSI works with single-master unwrapped interferograms. However, the unwrapped interferograms from both the SBAS and PSI can be interconverted. For instance, PSI interferograms can be transformed into multimaster interferograms [54]. On the other hand, unwrapped interferograms from the SBAS multimaster can be inverted to single-master unwrapped interferograms [55], [56], [57]. Consequently, the deformation estimation processes for the SBAS and PSI/DSI are essentially interchangeable at this stage [8].

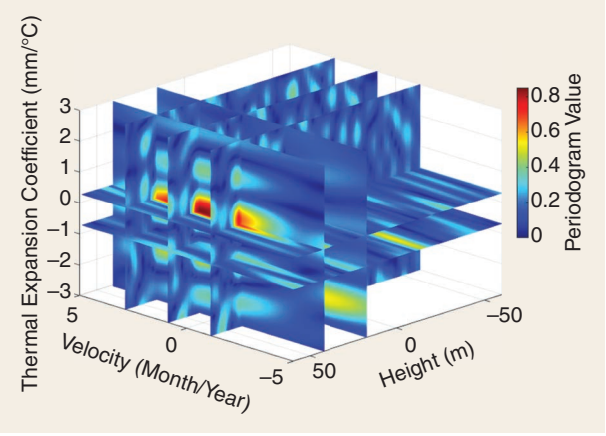

FIGURE 6. The MLE of PS parameters by grid-wise searching the periodogram.

PRE-ESTIMATION: STATISTICAL MODEL

Unlike the first two steps, which estimate parameters in the complex domain, estimating deformation from the unwrapped phase of interferograms is a problem in the real domain. The observation function can be expressed as follows:

$$\boldsymbol{\varphi} = \Phi(\boldsymbol{m}) + \boldsymbol{\varphi}_n. \tag{24}$$

Here, $\boldsymbol{\varphi}$ is the unwrapped phase; $\boldsymbol{\varphi}_n$ is the unmodeled noise, which includes instrument noise, atmospheric effects, signals from other scatterers, unwrapping errors, and deformation signals that are not captured by the model; and $\boldsymbol{m}$ includes the model parameters intended for unwrapped phase modeling, such as deformation parameters, topographic parameters, orbital parameters, and so on.

Generally, we can model $\boldsymbol{\varphi}_n$ as Gaussian noise; i.e.,

$$\boldsymbol{\varphi}_n \sim N(0, \sigma_{\boldsymbol{\varphi}}^2). \tag{25}$$

The pdf can be expressed as

$$f(\boldsymbol{\varphi} \mid \boldsymbol{m}) = (2\sigma_{\boldsymbol{\varphi}}^2\pi)^{-p} \exp\left(-\frac{1}{2\sigma_{\boldsymbol{\varphi}}^2}(\boldsymbol{\varphi} - \boldsymbol{\Phi}(\boldsymbol{m}))^H(\boldsymbol{\varphi} - \boldsymbol{\Phi}(\boldsymbol{m}))\right). \tag{26}$$

In summary, the statistical model for the deformation estimation problem is defined as

$$\begin{gathered}\text{Observation variable: } \boldsymbol{\varphi} \\ \text{Parameter variable: } \boldsymbol{m} \\ \text{pdf: } f(\boldsymbol{\varphi} \mid \boldsymbol{m}) \text{ in formula (26).}\end{gathered} \tag{27}$$

PARAMETER ESTIMATION

There are numerous methods to estimate the parameters once the phase data at the selected points have been unwrapped in all interferograms. The modeling of phase components due to orbit and topography is relatively consistent, with little variation. The primary distinction among these methods is how deformation is modeled. Broadly, there are two categories: those that do not use a deformation model and those that do. Without a deformation model, the deformation at each time point is treated as a parameter, making

Authorized licensed use limited to: Shaanxi Normal University. Downloaded on March 14,2024 at 04:23:51 UTC from IEEE Xplore. Restrictions apply.

the problem underdetermined. In contrast, when using a deformation model, a limited number of parameters describe the deformation over the time series, and in most cases, the problem is overdetermined.

For this underdetermined issue, nonparametric spatiotemporal filtering methods are typically employed. Often, the first step is to estimate elevation residuals and orbital errors. In the remaining residual phase, the deformation phase is then separated from the atmospheric phase and noise through filtering in both time and space. The underlying assumption is that deformation is correlated over time, the atmosphere is spatially correlated but not temporally, and noise is uncorrelated in both space and time.

Regarding parameter estimation algorithms, since the unmodeled noise is assumed to follow a Gaussian distribution, the problem can be directly addressed using least squares. However, due to the influence of unwrapping errors and other factors, outliers might arise. Consequently, some researchers prefer robust estimators over the least-squares estimator [58]. Additionally, since the atmospheric signal contributes significantly to the noise term, it is often required to remove the atmospheric phase screen (APS) before conducting deformation parameter estimation [59]. The APS can be estimated using the nonparametric spatiotemporal filtering method, external data source, or more advanced methods, as referenced in [60].

POSTESTIMATION

Nonparametric methods without a deformation model do not involve model verification and parameter quality assessment issues. Therefore, postestimation is suitable only for methods that have adopted a deformation model. Both model testing and quality assessment can be implemented.

Hypothesis testing methods are often taken to test and select deformation models. There are many choices for the deformation mode, such as the linear model, temperature-dependent model, exponential model, and so on. In practical applications, the hypothesis testing method can be designed according to the requirements of the scenario. For example, the augmented Dickey–Fuller (ADF) test method was proposed to test residuals in a bridge monitoring scenario [61]. For this study, the null hypothesis (H_0) being tested is the presence of a unit root, against alternative hypotheses (H_j). The ADF test generates a p value, which represents the likelihood of rejecting the null hypothesis. Typically, a p value lower than 5% indicates that the null hypothesis can be rejected, and thus, the time series is stationary. An alternative and more broadly applicable hypothesis testing method is the uniform test criterion for multiple hypotheses. The detection–identification–adaptation procedure is applied to enable multiple-hypothesis testing [62].

To assess the quality of estimated parameters of the deformation model, EP is an appropriate method when the parameter estimation is linear or approximately linear. To calculate the parameter variance from EP, accurate observation errors must be inputted. Although the original phase variance may be approximated from coherence [63], observation noise includes numerous contributions besides the original phase variance. Initial assumptions regarding the observation noise level may not be suitable. However, for a Gaussian distribution, observation variance can be estimated based on residual fitting of simulations. A simple model is to employ a covariance matrix with the same precision. Unbiased estimation of the precision parameters can then be achieved using the observation residual. If more complex covariance structures are required, the method of variance component estimation can be used to estimate the variance of grouped data [64]. Using the estimated variance of observations, the variance of parameters can be calculated based on the EP law. In a linear system, this is equivalent to the CRLB, as the least-squares estimator is the best linear unbiased estimator in such cases.

DIFFERENTIAL TOMOGRAPHIC SYNTHETIC APERTURE RADAR PARAMETER ESTIMATION

The previous sections primarily discussed the InSAR deformation measurement problem for single-mechanism scatterers. In scenarios like forests [65], [66], [67] and urban areas [68], [69], [70], there is often a phenomenon where multiple dominant scattering mechanisms are mixed within a single radar pixel. Thus, their parameter estimation issues differ from those previously discussed. Due to the complexity of the multimechanism aliasing problem, here, we limit our discussion to situations where mechanisms are distributed at different heights, which is the scenario where the D-TomoSAR method is applicable.

The estimation problem of D-TomoSAR involves determining the elevations and deformation parameters for all dominant scattering mechanisms within a single SAR pixel. The observation variable is the time series of the wrapped interferometric phase. This is similar to the PSI/DSI parameter estimation problem in 1D temporal unwrapping. The key distinction is that the parameter variables arise from multiple subresolution scatterers rather than from a single scatterer.

PRE-ESTIMATION: STATISTICAL MODEL

The observation variables and stochastic characteristics of the observation noise are the same as those in the PSI/DSI parameter estimation for 1D temporal unwrapping. This implies that formula (15) is also applicable in this context. Additionally, the atmospheric phase often constitutes a significant portion, complicating the estimation of model parameters. To reduce the disturbance, two methods can be employed. The first one involves using the arc observation, formed by making phase difference with a nearby single-mechanism PS pixel [58], to mitigate the atmospheric phase. The second approach involves initially estimating the APS of the interferogram and then directly removing it. A straightforward method is to employ the PSI technique to estimate the atmospheric phase of the PSs, followed by interpolating the APS of the interferogram [71].

Authorized licensed use limited to: Shaanxi Normal University. Downloaded on March 14,2024 at 04:23:51 UTC from IEEE Xplore. Restrictions apply.

In D-TomoSAR, the phase model is more complicated, as multiple scatterers should be considered. It is expressed as

$$\boldsymbol{\Psi}_k = \int_{s_l}^{s_u} \rho(s)\exp\left(-j2\pi\left(\xi_k s + \frac{2d(s,t_k)}{\lambda}\right)\right)ds \tag{28}$$

where $\rho(s)$ is the complex reflectivity profile along the elevation direction of that pixel, λ is the wavelength of the SAR system, $d(s,t_k)$ is the displacement as a function of the elevation and the acquisition time t_k, and s represents the elevation direction.

We discretize the continuous elevation variable s and deformation rate variable v in the search range, forming a 2D grid of size $M_s \times M_v$. The grid cells are stacked into a vector of size $M_s \times M_v$, and the elevation value and rate value of the cell with index n are denoted as s_n and v_n, respectively. The contribution of the grid cell $\boldsymbol{a}(s_n, v_n)$ to SAR observations can be expressed as

$$\boldsymbol{a}(s_n, v_n) = \exp(-j2\pi(\xi s_n + t v_n)) \tag{29}$$

where ξ and $\boldsymbol{t}$ are the baseline vector and time vector.

The integral in (28) can also be simplified as a matrix multiplication:

$$\boldsymbol{g} = \boldsymbol{\Psi}(\boldsymbol{\rho}) + \boldsymbol{w} = \boldsymbol{A}\boldsymbol{\rho} + \boldsymbol{w} \tag{30}$$

where $\boldsymbol{A} = [\ldots, \boldsymbol{a}(s_n, v_n), \ldots]$ has the steering vectors and $\boldsymbol{\rho}$ denotes the $M_s \times M_v$ reflectivity profile vector.

The conditional pdf for the wrapped phase given model parameters $\boldsymbol{\rho}$ is

$$f(\boldsymbol{g}\,|\,\boldsymbol{\rho}) = (2\sigma_w^2\pi)^{-p}\exp\left(-\frac{1}{2\sigma_w^2}(\boldsymbol{g}-\boldsymbol{A}\boldsymbol{\rho})^H(\boldsymbol{g}-\boldsymbol{A}\boldsymbol{\rho})\right). \tag{31}$$

Compared to the phase model used in temporal unwrapping, the D-TomoSAR phase model incorporates different parameters. While both consider the elevation and deformation information of the scatterers, D-TomoSAR accounts for scatterers in a continuous space. Since scatterers can exist at any position, the phase observation model corresponds to an infinite number of parameters. To render the model solvable, this continuous space must be discretized.

TABLE 2. THE DIFFERENCES AMONG THE SOLUTIONS FOR D-TomoSAR.

METHOD	OPTIMIZATION/LIKELIHOOD FUNCTIONS
Least squares	$\hat{\boldsymbol{\rho}} = (\boldsymbol{A}^H\boldsymbol{A})^{-1}\boldsymbol{A}^H\boldsymbol{g}$
L_1 regularization	$\hat{\boldsymbol{\rho}} = \text{argmin}\{\|\boldsymbol{g}-\boldsymbol{A}\boldsymbol{\rho}\|_2^2 + \alpha\|\boldsymbol{\rho}\|_1\}$
L_2 regularization	$\hat{\boldsymbol{\rho}} = \text{argmin}\{\|\boldsymbol{z}-\boldsymbol{A}\boldsymbol{\rho}\|_2^2 + \alpha\|\boldsymbol{L}\boldsymbol{\rho}\|_2^2\} = (\boldsymbol{A}^H\boldsymbol{A} + \alpha\boldsymbol{L}^H\boldsymbol{L})^{-1}\boldsymbol{A}^H\boldsymbol{g}$
Truncated singular value decomposition regularization	$\hat{\boldsymbol{\rho}} = \sum_{i=k_\alpha+1}^{M} \frac{\boldsymbol{u}_i^H\boldsymbol{g}}{\boldsymbol{\delta}_i}\boldsymbol{v}_i$
Beamforming	$\hat{\boldsymbol{\rho}} = \boldsymbol{A}^H\boldsymbol{g}$

As a result, the solution for the elevation and deformation parameters is transformed into the solution for the backscattering coefficient parameters of each discrete component of the observation.

In summary, the statistical model for D-TomoSAR parameter estimation is given by

$$\begin{gathered}\text{Observation variable: } \boldsymbol{g} \\ \text{Parameter variable: } \boldsymbol{\rho} \\ \text{pdf: } f(\boldsymbol{g}\,|\,\boldsymbol{\rho}) \text{ in formula (31).}\end{gathered} \tag{32}$$

PARAMETER ESTIMATION

Note that D-TomoSAR essentially uses limited observations to solve for continuous spatial parameters (in this case, a 2D continuous surface of the elevation and deformation rate). Therefore, parameter estimation is inevitably an ill-posed problem. The process of discretizing the continuous problem can also be considered a form of regularization, which confines the solution space within a finite range. The least-squares solution to the discretized linear problem is as follows:

$$\hat{\boldsymbol{\rho}} = (\boldsymbol{A}^H\boldsymbol{A})^{-1}\boldsymbol{A}^H\boldsymbol{g}. \tag{33}$$

However, using limited observations to solve for $M_s \times M_v$ backscattering coefficients may still result in an underdetermined problem, where the matrix $\boldsymbol{A}$ is rank deficient or close to rank deficient. Direct least-squares solutions to the problem above can lead to unstable solutions; i.e., the matrix $\boldsymbol{A}^H\boldsymbol{A}$ may exhibit numerical anomalies. Common regularization methods include truncated singular value decomposition [72], L_2 regularization (Tikhonov regularization), L_1 regularization, and so on. Additionally, although beamforming [73] is not considered a regularization method, we can see from the formula that it replaces $\boldsymbol{A}^H\boldsymbol{A}$ with the identity matrix, thereby avoiding the instability of matrix inversion and achieving the same effect as regularization (Table 2). Regularization can essentially be seen as a prior modeling of parameters, especially L_1 and L_2 regularization, which can also be expressed as an analytical prior probability expression. Therefore, parameter estimation based on regularization can to some extent be equivalent to Bayesian estimation.

Here, α is the regularization parameter, $\boldsymbol{L}$ is the Tikhonov/regularization matrix, $\boldsymbol{u}$ and $\boldsymbol{v}$ are the singular vectors of $\boldsymbol{A}$, $\boldsymbol{\delta}$ is the singular values, and k_α is the truncated number.

Because elevation scatterer points have spatial sparsity characteristics, L_1 regularization performs well in high-resolution interpretation (Figure 7) [74]. The least absolute shrinkage and selection operator is often used for processing. First, the iterative shrinkage thresholding algorithm is used for an iterative solution, and then model selection is performed. The iterative algorithm is as follows [75], [76]:

$$\begin{gathered}\hat{\boldsymbol{\rho}}_i = F(\hat{\boldsymbol{\rho}}_{i-1} + \mu\boldsymbol{A}^H(\boldsymbol{g}-\boldsymbol{A}\hat{\boldsymbol{\rho}}_{i-1}), \beta) \\ \text{with } F(\hat{\boldsymbol{\rho}}_i, \beta) = e^{j\angle(\hat{\boldsymbol{\rho}}_i)}\max(|\hat{\boldsymbol{\rho}}_i| - \beta, 0)\end{gathered} \tag{34}$$

where μ is the step-size and β is the threshold.

Authorized licensed use limited to: Shaanxi Normal University. Downloaded on March 14,2024 at 04:23:51 UTC from IEEE Xplore. Restrictions apply.

POSTESTIMATION

Model testing is a pivotal step in D-TomoSAR. Regardless of the regularization method employed for solving, a discrete range of heights will produce a certain number of nonzero values during the process. However, the presence of these nonzero values does not necessarily signify the existence of strong scattering objects at those heights. Different numbers and positions of scatterers correspond to various phase models. To identify the accurate model, researchers typically utilize model testing through hypothesis testing-based methods [77], [78] or information-theoretic criteria (ITC)-based methods [79], [80].

While D-TomoSAR is deemed capable of resolving more than two scattering objects, in practical applications, often, only up to two scattering objects are considered. The subsequent multiple-hypothesis test is formulated as follows [77]:

$$\begin{aligned} H_0&: \boldsymbol{g} = \boldsymbol{w} \\ H_1&: \boldsymbol{g} = \gamma_1 \boldsymbol{a}(s_1, v_1) + \boldsymbol{w} \\ H_2&: \boldsymbol{g} = \gamma_1 \boldsymbol{a}(s_1, v_1) + \gamma_2 \boldsymbol{a}(s_2, v_2) + \boldsymbol{w}. \end{aligned} \tag{35}$$

To determine which hypothesis to use, it is necessary to select the appropriate statistical measure for calculation and decision making. Commonly used statistical measures include the likelihood ratio and ensemble coherence. Existing research also indicates that if the intensity part of the observation $\boldsymbol{z}$ is normalized to one, then the two statistical measures, the ensemble coherence and likelihood ratio, are equivalent [78]. The likelihood ratio-based test can obtain better results than the coherence test that considers only phase information, as it considers both intensity and phase information simultaneously. Furthermore, in cases where only two hypotheses, H_0 and H_1, are necessary and the intensity is normalized, this hypothesis test can be simplified into temporal coherence criteria, which are widely used in PS selection.

Various methods are available for selection based on ITC, including the Bayesian information criterion (BIC), the Akaike information criterion, and the minimum description length. Although they share similar fundamental principles, their primary distinction lies in the penalty term used. Let $\hat{\boldsymbol{\rho}}_i$ denote the estimated vector of the unknown parameters with i scatterers. The general form of these information criteria can be represented as follows:

$$i = \operatorname{argmax}\{\ln f(\boldsymbol{g}; \hat{\boldsymbol{\rho}}_i, \mathcal{H}_i)\} - C(\hat{\boldsymbol{\rho}}_i)) \tag{36}$$

where $C(\,.\,)$ represents the penalizing function for parameter $\boldsymbol{\rho}$. A typical application scenario of D-TomoSAR is the monitoring of urban surface and infrastructure deformation because urban structures are complex, and one SAR pixel often contains multiple scatterers. The phase composition of the scatterers is also complicated, composed of elevation, temperature deformation, and trend deformation, among others.

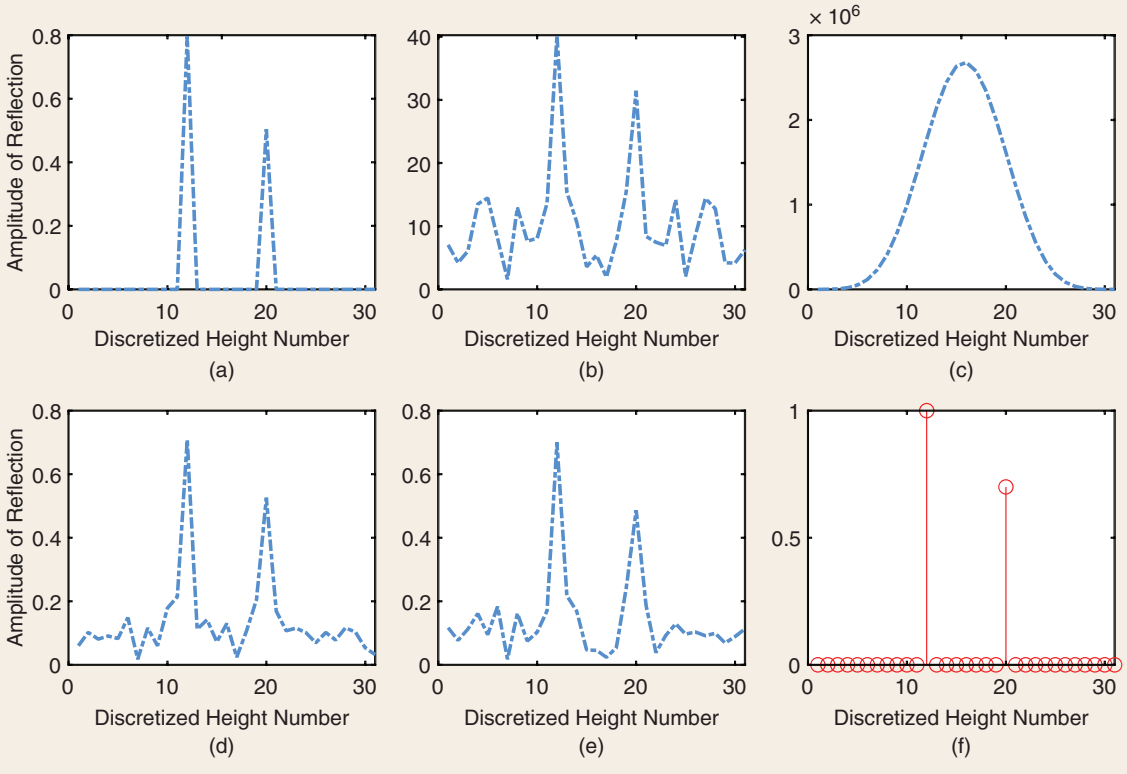

FIGURE 7. Reflectivity determination using different approaches. Blue dotted lines represent solved reflectivity profiles, and red circles indicate the ground truth. (a) Compressed sensing (L_1). (b) Beamforming. (c) Least squares. (d) L_2 regularization. (e) Truncated singular value decomposition. (f) Ground truth.

Authorized licensed use limited to: Shaanxi Normal University. Downloaded on March 14,2024 at 04:23:51 UTC from IEEE Xplore. Restrictions apply.

SUMMARY

We examined several primary parameter estimation problems associated with InSAR deformation measurement from the standpoint of statistical inference. For each problem, we detailed the statistical model, the estimation approach, and the postestimation procedure. These parameter estimation challenges encompass key issues in DSI, PSI, the SBAS, and D-TomoSAR. The first major distinction among these problems is whether the variables are in the complex domain or real domain. This distinction corresponds to different stochastic models and estimation approaches. The second significant difference lies in the scatterer type. The statistical models for DSs and PSs, as well as for single-dominant-mechanism scatterers and multiple-dominant-mechanism scatterers, differ significantly due to their inherent physical characteristics. The third notable discrepancy is whether the problem is underdetermined or overdetermined. For an underdetermined issue, an additional operation in terms of a simplified observation model or regularization must be made to enable a unique solution.

The objective of InSAR deformation measurement is to extract deformation signals from SAR observations. Since various deformation models are adopted for different application scenarios, the resulting outputs can vary. Figure 8

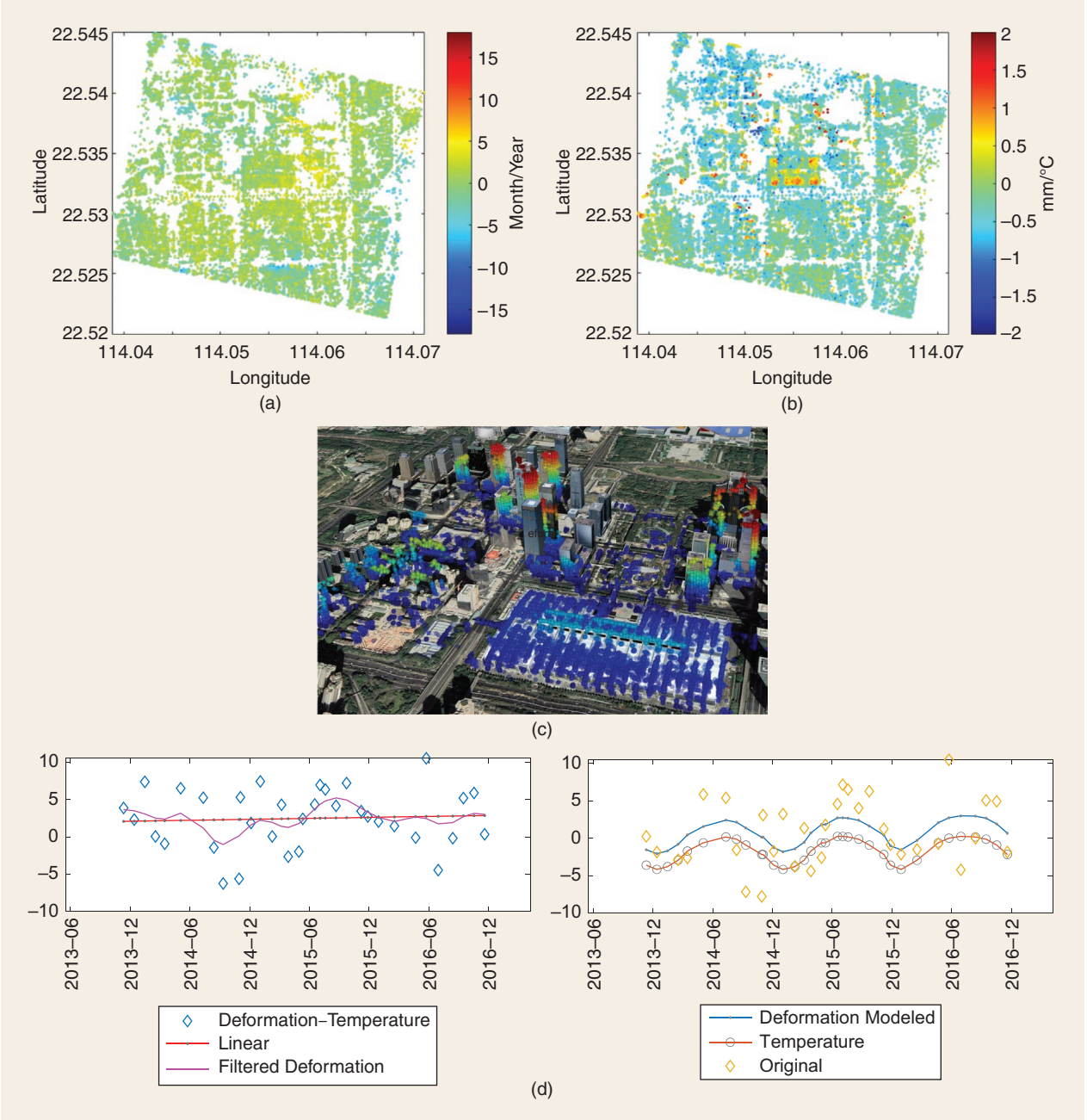

FIGURE 8. An InSAR outcome in an urban setting. The (a) linear velocity, (b) thermal expansion coefficients, (c) elevation map superimposed on a 3D model, and (d) components of the InSAR time series.

Authorized licensed use limited to: Shaanxi Normal University. Downloaded on March 14,2024 at 04:23:51 UTC from IEEE Xplore. Restrictions apply.

presents an example of monitoring outcomes for PS points within an urban setting. In this context, considerations for thermal expansion and height residuals from a digital elevation model are essential for urban infrastructure. The outcomes include the results for elevation parameters, thermal expansion coefficient parameters, linear deformation parameters, and the time series data of deformation components.

STATISTICAL INFERENCE IN INTERFEROMETRIC SYNTHETIC APERTURE RADAR-CONSTRAINED GEOPHYSICAL INVERSION

Compared to InSAR deformation measurement, InSAR-constrained geophysical parameter estimation follows a somewhat straightforward framework. The stochastic model for InSAR displacement remains consistent across all geophysical inversion scenarios. Consequently, the structure of this section differs slightly from the section on deformation measurement. This entire section can be viewed as a single type of estimation problem, and we delve into pre-estimation, estimation, and postestimation in each part. During pre-estimation, we first examine the common function models used in InSAR-constrained geophysical inversion, followed by a presentation of the stochastic characteristics of InSAR measurements. In the part covering estimation, we outline the parameter estimation process based on the types of parameters involved, distinguishing between linear and nonlinear parameter estimation. In postestimation, we discuss quality evaluation indicators and methods relevant to the inversion results.

PRE-ESTIMATION: STATISTICAL MODEL

FUNCTION MODEL IN INTERFEROMETRIC SYNTHETIC APERTURE RADAR-CONSTRAINED GEOPHYSICAL INVERSION

In InSAR-constrained geophysical inversion, the input typically includes three types of measurements: displacement map, velocity map, and displacement time series. However, using time series displacements for inversion is not common, as the derivation of time series displacement is already based on some deformation models with specific spatiotemporal deformation characteristics. MT-InSAR analysis can sometimes be insufficient for distinguishing complicated geophysical processes, such as random aftershock deformation in postseismic deformation maps, so it is essential to examine the data carefully before directly using MT-InSAR results for analysis. When multitemporal inversion is necessary, there are two possible strategies. The first is to use the differential InSAR interferogram and manually select the appropriate data, while the second is to use the velocity map for deformation scenarios that can be adequately explained by a linear deformation model.

The inversion problem can be described the same way for all kinds of other geophysical problems, with the general formula [81]

$$\mathbf{d} = \mathcal{A}(\mathbf{m}) + \boldsymbol{\varepsilon} \tag{37}$$

where $\mathcal{A}$ is the operator function for the forward model, $\mathbf{m}$ is the vector of model parameters, $\mathbf{d}$ is the observation data, and $\boldsymbol{\varepsilon}$ is the observation error.

Deformation models $\mathcal{A}(\mathbf{m})$ provide the linkage between crustal deformation and the source underground. The existing models can be grouped into three types: analytical model, semianalytical model, and numerical model. The analytical model was the earliest model, giving ground displacement due to an embedded source in the homogeneous half-space. However, geological and geophysical data all suggest that Earth's crust is not a homogeneous layer, which has been assumed in analytical models. Therefore, semianalytical models with the consideration of a layered Earth structure were proposed. Differing from the homogeneous half-space, the kernel functions in the stratified case cannot be acquired analytically. Some mathematical methods, like numerical integration [82], [83] or approximation by a finite series of Lipschitz–Hankel integrations [84], were used to give the semianalytical solution. If more detailed considerations, like the complex geometry, lateral variation, or a rigid layer, are required, we need to resort to the third type of deformation model, numerical models, including the finite-element model (FEM) and boundary element model, between which the FEM has been applied more widely, e.g., in [85], [86], and [87].

InSAR geophysical inversion is widely used in various fields, with earthquake and volcano deformation being the most common. Other applications include underground water exploitation, underground mineral resource development, permafrost changes, and glacier activities.

Earthquakes occur when there is a sudden release of built-up energy within the crust, typically along fault lines. This sudden release of energy causes the rock on either side of the fault to rapidly move relative to the opposing side,

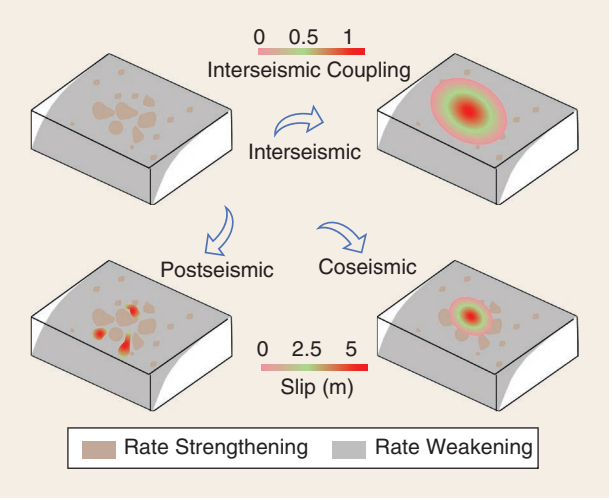

FIGURE 9. Different stages of the earthquake cycle. The fault region includes both rate weakening and rate strengthening areas. This distribution influences interseismic locking, coseismic rupture, and postseismic afterslip, with corresponding surface deformation patterns observable by InSAR [88].

Authorized licensed use limited to: Shaanxi Normal University. Downloaded on March 14,2024 at 04:23:51 UTC from IEEE Xplore. Restrictions apply.

resulting in deformation of the surface [88]. The Okada model has been the most widely accepted model for fault slip modeling [89]. The model is based on the theory of linear elasticity and considers the crust a homogeneous, isotropic, and elastic solid. The model considers the geometry of the fault, the orientation of the fault plane, and the properties of the rock surrounding the fault. The Okada model predicts the displacement and strain of the crust caused by the movement of tectonic plates, including earthquakes. It has been widely used to study the behavior of faults and to estimate the degree of the seismic hazard in a particular region.

The Okada model can account for various mechanisms in different stages of the earthquake cycle, such as interseismic locking, coseismic rupture, and postseismic afterslip (Figure 9). However, some nonelastic processes in the postseismic phase, such as viscoelastic relaxation and poroelastic rebound, require other types of analytical models to explain them, such as power law models [90] for viscoelastic relaxation and effective medium models [91] for poroelastic rebound. Moreover, some earthquakes involve complex geometry, rigid layers, or significant lateral variation that affect deformation modeling but cannot be handled by analytical or semianalytical models [85], [86], [87]. Therefore, numerical models are needed to address this kind of problem.

The deformation mechanism of a volcano involves the movement and pressure changes of magma beneath the surface of Earth, causing the ground above to swell, contract, or shift, leading to noticeable changes in the volcano shape. The Mogi model is a one of the most popular models in volcano deformation modeling, and it assumes a spherical magma chamber in an elastic, homogeneous, and isotropic medium. The model relates the surface displacement to the volume change of the magma chamber using a closed-form solution based on the theory of dislocations (Figure 10).

The Mogi model can be expressed as

$$u_r = \frac{\alpha^3 \Delta P(1-\nu)}{G}\frac{x}{R^3}$$
$$u_z = \frac{\alpha^3 \Delta P(1-\nu)}{G}\frac{D}{R^3}. \tag{38}$$

Here, u_r and u_z are the horizontal radial and vertical displacements at the surface, x is the horizontal radial distance, G is the shear modulus of the medium, D is the depth of the magma chamber center, $R = \sqrt{x^2 + D^2}$ is the distance from the magma chamber center to any point on or above the surface, ν is Poisson's ratio, and ΔP is the source overpressure [92].

The Mogi model can be used to explain some features of volcanic deformation, such as uplift, subsidence, and horizontal motion. However, it has some limitations, such as neglecting topography effects, layered media effects, and nonspherical source shapes [93]. The Okada model can be taken for the finite rectangular dislocation model [89]. Additionally, an exact analytical solution for the finite ellipsoidal source model was derived and successfully applied to parameter inversion for the Kilauea volcano [94]. Based on these three basic models—Mogi, Okada, and Yang—other models have been developed, such as flattened disc-shaped, closed (or open) conduit, and composite dislocation models with higher degrees of freedom, among others [93], [95]. These simple and effective analytical models for volcanic activity have been widely used in the study of volcanic motion systems at plate boundaries, including magma chamber parameters, intrusion processes, the spatiotemporal distribution of magma eruptions, and the coupling relationship between volcanic eruptions and fault movements [96], [97].

Numerical models have also been adopted for modeling volcanic systems due to their flexibility [92]. This approach allows us to assess the effects of complexities such as nonelastic rheology [98], layering and faulting [99], and topography [100]. However, creating complex realistic numerical models often requires ground-collected data that are not available. Moreover, directly inverting displacement fields within numerical models is usually complex, so analytical models are often used to approximate source parameters first. Then, these initial analytical results are used within a numerical model that could incorporate heterogeneity, topography, and anelastic rheology to constrain the best-fitting source [101].

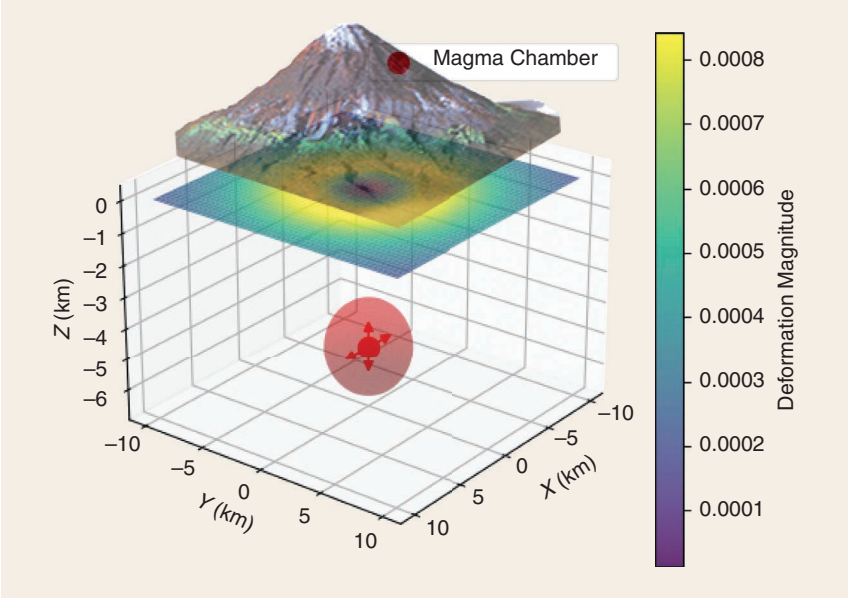

FIGURE 10. A visualization of the Mogi model for volcanic deformation. The expansion of a spherical magma chamber at depth results in elliptical deformation at the surface.

Authorized licensed use limited to: Shaanxi Normal University. Downloaded on March 14,2024 at 04:23:51 UTC from IEEE Xplore. Restrictions apply.

Besides earthquake and volcano activities, there are many other activities and objects that can result in ground deformation and be observed by InSAR:

- *Groundwater overexploitation*: Disasters such as ground subsidence, ground fissures, and seawater intrusion can be caused by groundwater overexploitation. InSAR can obtain a high-resolution surface deformation field, establish a function model of surface deformation and groundwater change, and detect physical characteristics of groundwater change and invert corresponding aquifer parameters, providing a new perspective for hydrogeological applications. Hydrogeological parameter inversion uses InSAR-observed seasonal/interannual deformation data and a certain amount of groundwater well data. Combined with soil mechanics, stress–strain, and other theoretical models, it can identify and invert a series of hydrogeological parameters [102], [103].
- *Underground goaf*: The goaf left behind after underground mineral resource exploitation is prone to cause a series of disasters. For example, the overlying rock mass of a goaf can easily produce movement deformation due to losing support, which leads to geological disasters, such as surface subsidence and infrastructure damage. InSAR observation can constrain the inversion of underground goaf geometric parameters [104], such as location, depth, length, width, thickness, dip angle, azimuth angle, and so on.
- *Frozen soil active layer*: InSAR technology can accurately obtain surface deformation in frozen soil areas, providing an observation basis for large-scale high-precision inversion of frozen soil physical parameters (such as melting depth and active layer thickness) [105], [106]. A series of models were built to link InSAR surface deformation and active layer thickness in frozen soil areas, estimating multiyear frozen soil active layer thickness glacier surge parameter inversion.

STOCHASTIC CHARACTERISTICS FOR INTERFEROMETRIC SYNTHETIC APERTURE RADAR OBSERVATION

The noise $\boldsymbol{\epsilon}$ in InSAR measurements is normally assumed to be of a Gaussian type and described by a covariance matrix $\boldsymbol{\Sigma}$. The pdf follows:

$$f(\boldsymbol{d}|\mathbf{m}) = \frac{1}{(2\pi)^{\frac{n}{2}}\boldsymbol{\Sigma}^{\frac{1}{2}}} \exp\left(-\frac{1}{2}(\boldsymbol{d}-\mathcal{A}(\mathbf{m}))^T\boldsymbol{\Sigma}^{-1}(\boldsymbol{d}-\mathcal{A}(\mathbf{m}))\right). \tag{39}$$

Please note that the observation $d_i \in \boldsymbol{d}$ denotes the InSAR measurement at pixel i. It differs from the time series InSAR measurement vector that uses the subscript to represent the time. The uncertainty of the InSAR results sometimes would be derived simultaneously during InSAR data processing, and the variance is usually estimated on a per-pixel basis. However, the geophysical process is particularly concerned with the spatial stochastic characteristics, that is, the covariance between neighboring pixels, rather than the covariance among measurements of a pixel at different times. Therefore, an additional step is typically required to estimate the error statistics in the InSAR data.

To estimate the error variances and autocovariances in InSAR data, a common approach is to select an area in the interferograms where no geophysical deformation signal is expected or visible. The assumption is that the error statistics in the nondeforming areas are the same as those in the adjacent deforming areas and that the errors are stationary. The size of the selected area should be similar to that of the investigation area to ensure that the whole bandwidth of periods present in the noise is captured. One method for estimating InSAR variances is to use sample semivariograms, while sample covariograms can be used to estimate spatial correlation in the data [107]. The discrete sample semivariogram value for the kth distance class is

$$\hat{\gamma}(h_k) = \frac{1}{2N} \sum_{\substack{i=1 \\ \|\boldsymbol{r}_i - \boldsymbol{s}_i\| \cong h_k}}^{N} [\boldsymbol{d}(\boldsymbol{r}_i) - \boldsymbol{d}(\boldsymbol{s}_i)]^2 \tag{40}$$

where h_k is the distance for the kth class and N is the number of data point pairs at locations $\boldsymbol{r}_i$ and $\boldsymbol{s}_i$. The distance between them is approximately h_k. Under the assumption of isotropic noise, the semivariogram is solely dependent on the distance h between data points, while the sample covariogram can be expressed as

$$\hat{C}(h_c) = \frac{1}{2N} \sum_{\substack{i=1 \\ \|\boldsymbol{r}_i - \boldsymbol{s}_i\| \cong h_c}}^{N} \boldsymbol{d}(\boldsymbol{r}_i)\boldsymbol{d}(\boldsymbol{s}_i). \tag{41}$$

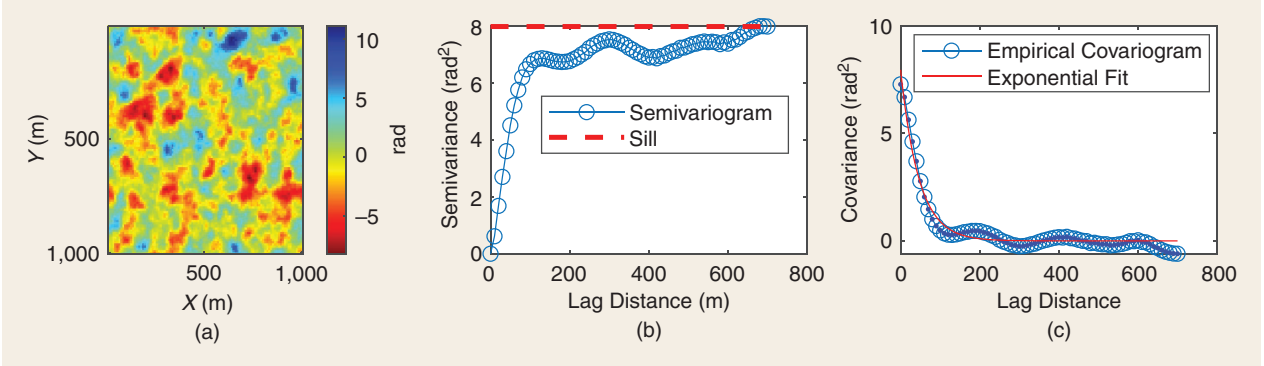

FIGURE 11. An (a) InSAR noise map, (b) empirical semivariogram, and (c) empirical covariogram.

Authorized licensed use limited to: Shaanxi Normal University. Downloaded on March 14,2024 at 04:23:51 UTC from IEEE Xplore. Restrictions apply.

In order to describe the covariances continuously, we fit functions to the sample covariogram. We select function types that guarantee positive definiteness, which is required by the definition of covariance [108]. Two examples of such functions are

$$C(h)=\begin{cases} s & h=0 \\ be^{-h/a} & h>0 \end{cases}$$
$$C(h)=\begin{cases} s & h=0 \\ be^{-h/a}\cos(h/c) & h>0. \end{cases} \tag{42}$$

Here, a, b, and c are the coefficients for the model, and s is the sill given by the semivariogram. The decay of correlation with distance is represented by the exponential function $e^{-h/a}$, while the anticorrelation in certain scenarios is depicted by $\cos(h/c)$. Figure 11 is an example of InSAR noise structure estimation.

In summary, the statistical model for InSAR-constrained geophysical inversion is defined as

$$\begin{gathered} \text{Observation variable: } \boldsymbol{d} \\ \text{Parameter variable: } \boldsymbol{m} \\ \text{PDF: } f(\boldsymbol{d}|\boldsymbol{m}) \text{ in formula (39).} \end{gathered} \tag{43}$$

PARAMETER ESTIMATION

BASICS

When conducting geophysical inversion based on geodetic data, geophysical parameters can be divided into two categories: nonlinear parameters and linear parameters [109]. Linear parameters typically correspond to the motion parameters of underground sources in elastic media, such as fault slip and magma chamber volume changes. In contrast, nonlinear parameters generally relate to the geometric or material parameters of the source and medium, including point source location, fault dip angle, fault strike, viscoelastic coefficient, Poisson's ratio, and so on. When the underground source extends over a specific volume or area, grid division is needed to achieve higher spatial resolution of the motion source distribution. In such situations, the number of linear parameters may exceed the amount of observation data, resulting in an ill-posed problem for parameter estimation (Figure 12). Consequently, the primary distinctions in parameter estimation depend on the linear or nonlinear nature of the parameters. In this section, we separately discuss nonlinear parameter estimation, linear parameter estimation, and mixed-parameter estimation.

NONLINEAR PARAMETER INVERSION

Nonlinear parameter inversion is utilized when the number of unknown parameters is limited and the linear parameters remain undiscretized. In this situation, the operator A is nonlinear, and obtaining an analytical optimal solution for the unknown parameters, as in a linear problem, is not feasible. The most straightforward approach to addressing this issue is by linearizing the parameters. This step involves initializing the parameter values based on a priori knowledge:

$$\mathbf{m}_0^T=(m_{10},\ldots,m_{J0}). \tag{44}$$

Using a Taylor series to expand the right part of function model gives

$$\begin{aligned} \mathrm{d}_i=\mathcal{A}_i(\boldsymbol{m}_0)&+\sum_{j=1}^{J}\left[\frac{\partial\mathcal{A}_i}{\partial m_j}\right]_{m_{j0}}(m_j-m_{j0}) \\ &+\sum_{j=1}^{J}\left[\frac{\partial^2\mathcal{A}_i}{\partial m_j^2}\right]_{m_{j0}}\frac{(m_j-m_{j0})^2}{2!}+\cdots. \end{aligned} \tag{45}$$

By ignoring terms above the first order, the nonlinear problem can be approximated by a linear formula:

$$\boldsymbol{y}=\boldsymbol{J}\boldsymbol{x} \tag{46}$$

where

$$\begin{aligned} &\boldsymbol{y}\text{: } y_i=\Delta d_{i0}=d_i-A_i(\boldsymbol{m}_0),\ i=1,\ldots,n \\ &\boldsymbol{x}\text{: } x_i=\Delta m_{j0}=m_j-m_{j0},\ j=1,\ldots,J \\ &\boldsymbol{J}\text{: Jacobian matrix with each element: } g_{ij}=\left[\frac{\partial A_i}{\partial m_j}\right]_{m_{j0}}. \end{aligned}$$

Equation (46) can be solved using the linear least-squares method. The obtained $\boldsymbol{x}$ is added to the initial parameter $\boldsymbol{m}_0$ to update it to $\boldsymbol{m}_0+\boldsymbol{x}$. This linearization and inversion process is repeated until $\boldsymbol{x}$ reaches a certain threshold (Figure 13). The steepest descent method, which is a gradient-type method, is used to achieve this.

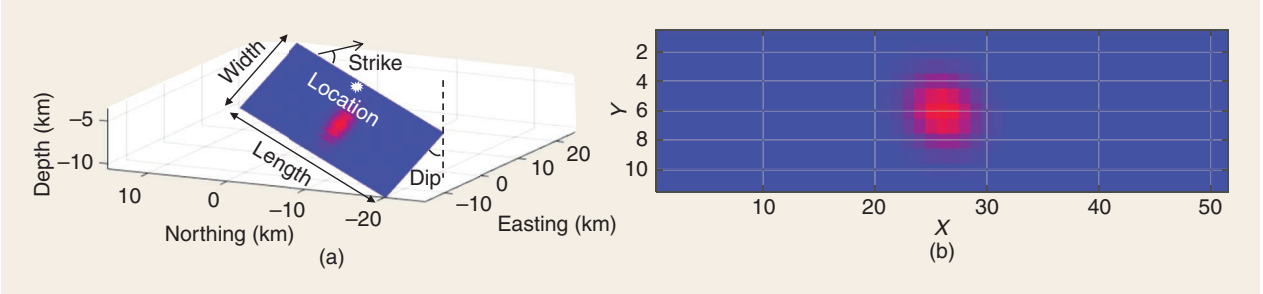

FIGURE 12. Nonlinear and linear parameters in an earthquake fault dislocation model. (a) Nonlinear parameters typically encompass the strike, width, location, length, and dip of a fault plane. (b) Linear parameters refer to the slips of all discretized fault patches.

Authorized licensed use limited to: Shaanxi Normal University. Downloaded on March 14,2024 at 04:23:51 UTC from IEEE Xplore. Restrictions apply.

The method provides a local minimum around $\boldsymbol{m}_0$. Other gradient-type methods, such as the Newton method and the conjugate gradient method, also provide the local minimum but in a different way. There are also nonlinear inversion methods that search for the global minimum, such as the genetic algorithm, the simulated annealing method, and artificial neural networks. For more details about these nonlinear methods, several works in the literature can be referred to [81], [110], [111], [112], [113].

Besides the linearization way, the Markov chain Monte Carlo (MCMC) method within the Bayesian framework is another commonly used approach for solving nonlinear parameters [114]. This approach directly provides the posterior pdf and is suitable for complex scenarios. The Metropolis–Hastings algorithm is used to efficiently control the sampling process such that after a large number of iterations, the sample density approximates the posterior distribution. To begin, an initial set of model parameters, denoted as $\boldsymbol{m}_0$, are selected from the prior distribution $f(\boldsymbol{m})$. This can be arbitrarily chosen or previously estimated using a direct search method, such as simulated annealing. Next, a new trial set of model parameters is generated by taking a random step within $f(\boldsymbol{m})$. If the prior for each model parameter is uniform and independent, this can be achieved by perturbing each parameter in $\boldsymbol{m}_i$ by an amount $a_n \Delta m^j$, where a_n is a random value generated from a uniform distribution within the range [–1, 1] and Δm^j is the maximum random walk step-size for each parameter m^j. An acceptance ratio $r = \min(1, f(\boldsymbol{d}|\boldsymbol{m}_{i+1})/f(\boldsymbol{d}|\boldsymbol{m}_i))$ is then calculated and compared with a random value u generated from a uniform distribution within the range [0, 1]. If $u < r$, the trial set is accepted. Otherwise, the previous set of model parameters is retained by setting $\boldsymbol{m}_{i+1} = \boldsymbol{m}_i$. The resulting sequence of states, $\boldsymbol{m}_0, \boldsymbol{m}_1, \boldsymbol{m}_2, \ldots$, forms a Markov chain with the target distribution $f(\boldsymbol{m}|\boldsymbol{d})$ as its stationary distribution. The process is repeated until a representative sampling of the posterior distribution is achieved (Figure 14).

In general, the nonlinear parameter $\boldsymbol{m}$ in geophysical inversion often lacks prior information, and the prior probability can be modeled as the so-called uninformative Jeffreys prior, i.e., a uniform distribution over the real number field. However, if there is a finite range of values, $f(\boldsymbol{m})$ can be considered a uniform distribution with upper and lower bounds. In such cases, when generating a new set of parameters in the first step of the MCMC, a preprocessing step is required. If the new parameter set $\boldsymbol{m}_{i+1}$ falls outside the value range, a wrapping operation can be performed to convert it back into the acceptable range.

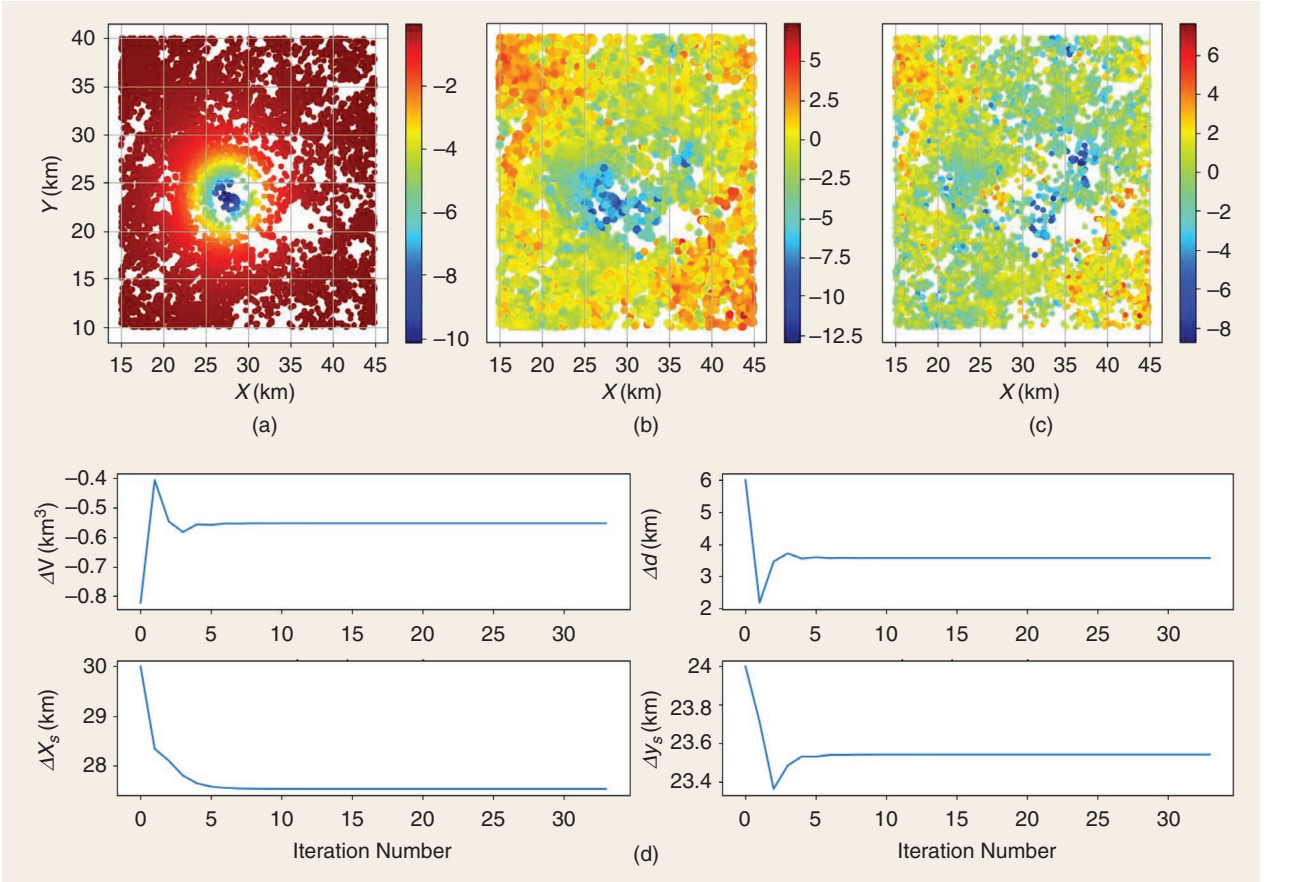

FIGURE 13. Inverting volcano deformation involves linearizing the parameters. (a) Modeled deformation. (b) Observed deformations by InSAR. (c) Residuals between the model and observation. (d) The convergence of estimated parameters in the Mogi model along with the iteration number.

Authorized licensed use limited to: Shaanxi Normal University. Downloaded on March 14,2024 at 04:23:51 UTC from IEEE Xplore. Restrictions apply.

LINEAR PARAMETER INVERSION

When the nonlinear parameters are assumed to be known and the linear parameters are spatially discretized, the parameter solving process transforms into a linear inversion. In cases where a priori knowledge about the parameters is lacking, the solution can be determined through MLE, which equates to the least-squares solution. However, inverting the spatial distribution of subsurface linear motion parameters using surface observations is frequently an ill-posed problem. The number of discretized parameters may surpass the number of observed data points, and surface deformation might not be sensitive to deep movements. Consequently, incorporating additional prior probabilities for the discretized linear parameters becomes essential.

Laplacian smoothing is a commonly adopted approach for regularization [115]. Laplacian smoothing minimizes the sum of the second spatial derivatives, thereby seeking to keep the difference in the slip between patches small. A prior based on Laplacian smoothing is given by

$$f(\boldsymbol{m}) = \frac{1}{(2\pi\alpha^2)^{\frac{n}{2}}} |\boldsymbol{L}^T\boldsymbol{L}|^{1/2} \exp\left(-\frac{1}{2\alpha^2}(\boldsymbol{Lm})^T(\boldsymbol{Lm})\right) \quad (47)$$

where α^2 is a hyperparameter controlling the slip variance and $\boldsymbol{L}$ is a matrix that represents the finite-difference approximation of the Laplacian operator.

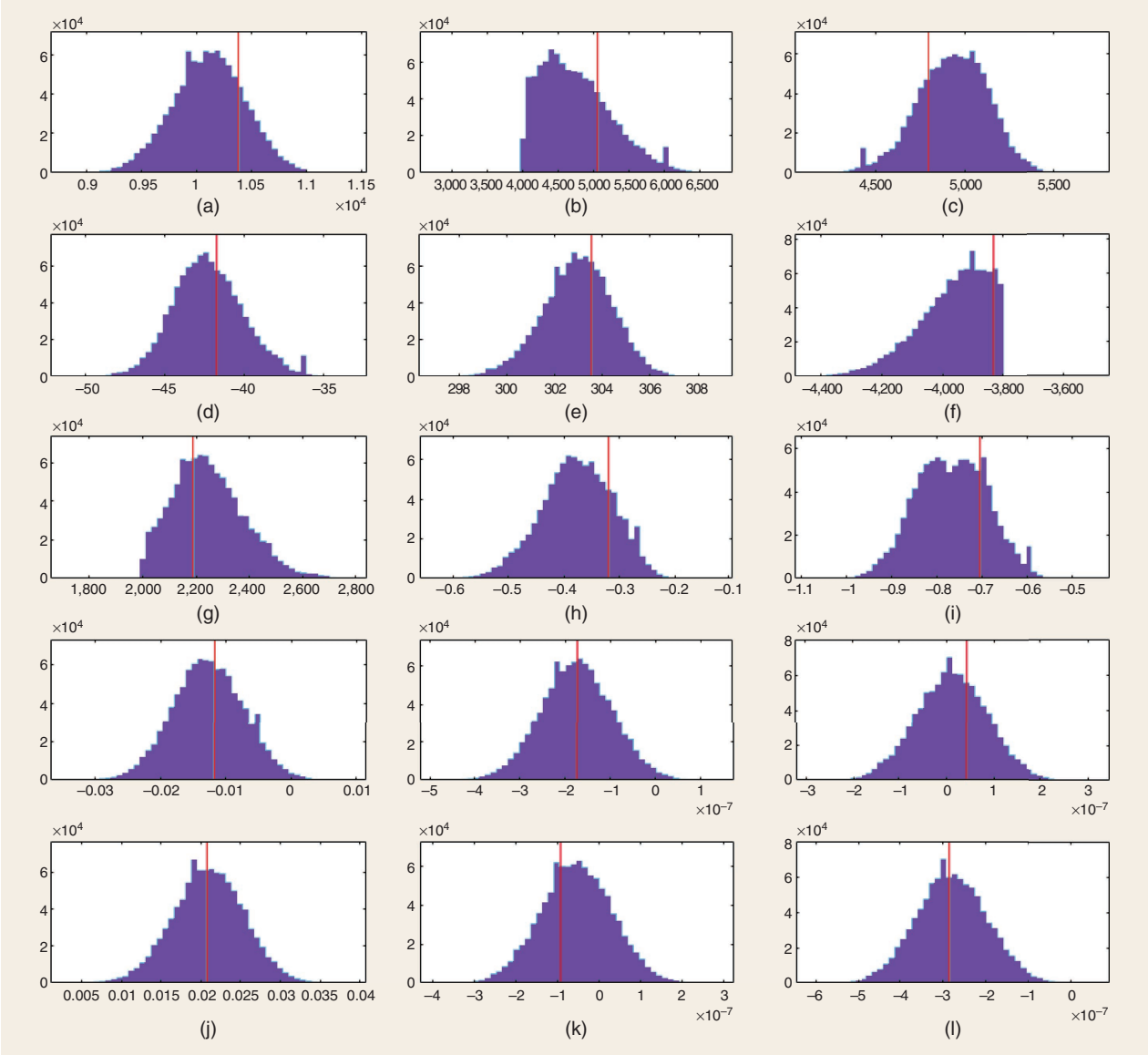

FIGURE 14. Estimating the fault geometric parameters and InSAR ramp parameters of the 2017 Mashhad earthquake (moment magnitude 6.1) using the MCMC. The fault geometric parameters to be solved include the fault (a) length, (b) width, (c) depth, (d) dip, (e) strike, (f) location X, (g) location Y, (h) strike slip, and (i) dip slip. The InSAR ramp parameters include a (j) constant, (k) ramp slope in the *x* direction, and (l) ramp slope in the *y* direction for two InSAR datasets. The purple histogram and red line indicate the posterior probabilities and optimal values.

Authorized licensed use limited to: Shaanxi Normal University. Downloaded on March 14,2024 at 04:23:51 UTC from IEEE Xplore. Restrictions apply.

Assuming $\mathbf{\Sigma} = \sigma^2 Q$, according to Bayesian formulation, the post-pdf of the slip is given by

$$f(\boldsymbol{m}\,|\,\mathbf{d}) \propto \frac{1}{\sigma^2}(\mathbf{G}\boldsymbol{m}-\mathbf{d})^T Q^{-1}(\mathbf{G}\boldsymbol{m}-\mathbf{d}) + \frac{1}{\alpha^2}\boldsymbol{m}^{\mathrm{T}}\mathbf{L}^{\mathrm{T}}\mathbf{L}\boldsymbol{m}. \quad (48)$$

By introducing $\lambda = \sigma^2/\alpha^2$, the parameter inversion becomes the following optimization problem:

$$\begin{aligned}\hat{\boldsymbol{m}} &= \operatorname{argmin}\{(\mathbf{G}\boldsymbol{m}-\mathbf{d})^T Q^{-1}(\mathbf{G}\boldsymbol{m}-\mathbf{d}) + \lambda \boldsymbol{m}^{\mathrm{T}}\mathbf{L}^{\mathrm{T}}\mathbf{L}\boldsymbol{m}\} \\ &= (\mathbf{G}^T Q^{-1}\mathbf{G} + \lambda^2 \mathbf{L}^T\mathbf{L})^{-1}\mathbf{G}^T\mathbf{Q}^{-1}\mathbf{d}. \end{aligned} \quad (49)$$

Figure 15 gives an example of solving the linear slip parameters on fault patches for an earthquake sequence using the Laplacian smoothing. An alternative to regularization by Laplacian smoothing is regularization by constraining the slip distribution to be self-affine [9]. For example, the von Karman prior was used in fault slip regularization. In this study, the von Karman autocorrelation function was adopted to calculate the autocorrelation matrix Q_m for slip on the fault patches. The von Karman prior is given as

$$f(\boldsymbol{m}) = \frac{1}{(2\pi\alpha^2)^{\frac{n}{2}}\,|\mathbf{Q}_m|^{\frac{1}{2}}} \exp\left(-\frac{1}{2\alpha^2}(\boldsymbol{m})^T Q_m^{-1}(\boldsymbol{m})\right). \quad (50)$$

The analytical solution for $\boldsymbol{s}$ can also be given the same way. We note that a scalar smoothing factor controls the weight of this smoothing. Its value is usually determined by iterating the inversion for different factors, computing the misfit, and constructing an "L curve" of the smoothing factor versus the misfit. The tradeoff approach is employed the most, often without justification. Information criteria have been introduced to provide an objective determination of the smoothing factor, as a range of potential solutions may exist. Akaike's BIC (ABIC) is a widely used objective method based on the entropy maximization principle that determines a suitable smoothing factor [116], [117].

MIXED-PARAMETER INVERSION

In real scenarios, it is common to encounter a mix of linear and nonlinear parameters that need to be solved simultaneously. This requires the development of a robust mixed-parameter inversion procedure that can accurately estimate both types of parameters. Currently, there are generally three types of inversion procedures that can handle mixed parameters.

The first one is a two-step procedure and was proposed the earliest, and it has been commonly applied [118], [119], [120], [121], [122]. This method involves solving for the nonlinear and linear parameters in separate steps. First, the nonlinear source geometry is determined using a nonlinear inversion method under the assumption of a uniform source on a fixed point or a rectangular surface. Second, the usual linear inversion is applied to solve for discretized parameters (e.g., slips on fault patches), with the geometry given by the first step. The advantage of this procedure is that the inversion process is easy to handle since the complicated inversion problem is divided into two simple steps, both of which can be solved by numerous mature methods. However, the results obtained from this method may not be robust enough since the geometry obtained in the first step is based on the assumption of a uniform source. For simple

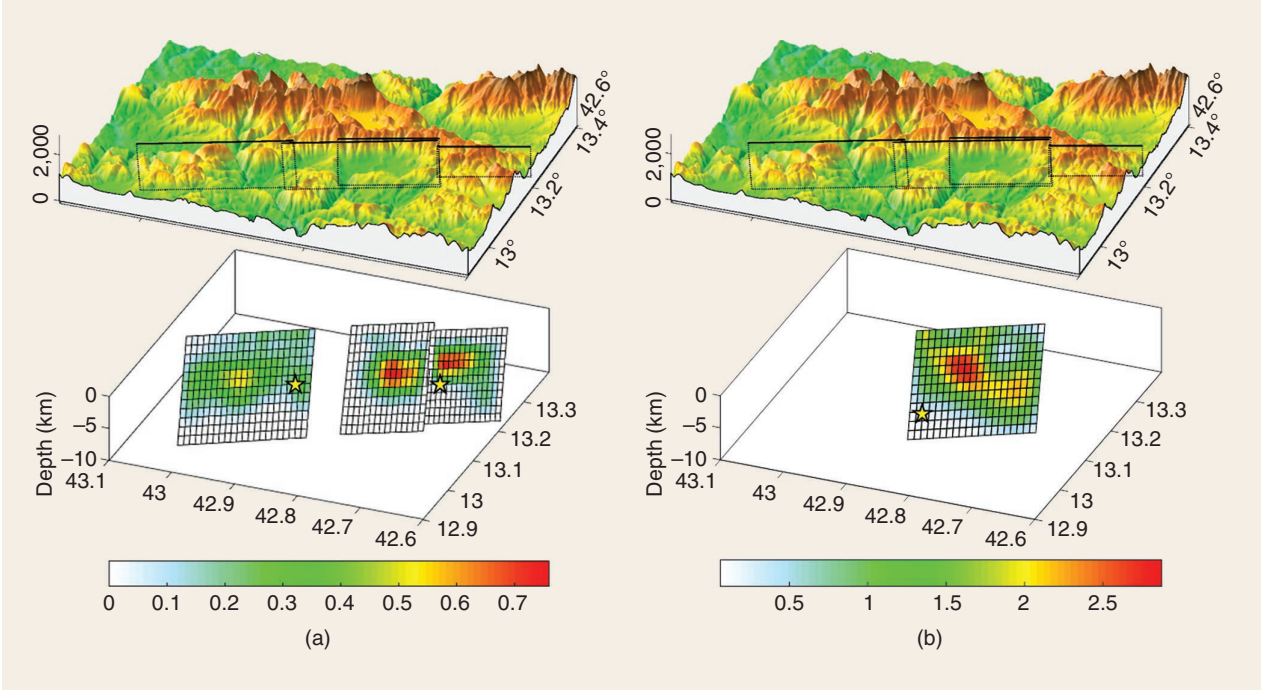

FIGURE 15. Linear slip distribution inversion results for the 2016 Central Italy earthquake sequence, with yellow stars indicating the rupture initiation points. (a) The 24 August 2016 Visso (left) and 26 October 2016 Amatrice (right) earthquakes. (b) The 30 October 2016 Norcia earthquake.

Authorized licensed use limited to: Shaanxi Normal University. Downloaded on March 14,2024 at 04:23:51 UTC from IEEE Xplore. Restrictions apply.

scenarios, e.g., earthquakes with only one slip concentration on a single fault plane, the first step may generate a nearly correct geometry. However, for more complex cases, the inverted geometry may deviate significantly from the real situation. Additionally, the uncertainties of nonlinear parameters obtained in the first step could propagate into the second step, resulting in an incorrect inversion result.

The second one is a mixed procedure, which combines the inversion of linear slip and nonlinear geometry and has been proposed to improve the accuracy of parameter solving [109], [117], [123], [124]. This procedure uses an iterative algorithm in the least-squares framework [123]. First, the nonlinear parameters are initialized based on a priori knowledge, such as field surface rupture maps, SAR offset maps, and aftershock locations. Then, preliminary linear parameters and the misfit between the observation and prediction are obtained through a linear inversion. The linear inversion is iterated by gradually modifying the initial nonlinear parameters. If the data fitting improves to an expected value, the changes of the nonlinear parameters are accepted. After the iteration, the best-fitting solution during the search process is obtained. Alternatively, the nonlinear parameters can be introduced as hyperparameters, and information criteria are used to determine the optimal values [117]. The inversion performs a forward grid search for the best-fitting solution. For each set of candidate nonlinear parameters, Green functions are recalculated to obtain an ABIC value. After all the calculations are completed, the minimum ABIC is found, and its corresponding parameters are selected as the optimal solution.

The third inversion procedure type is fully nonlinear inversion, which brings nonlinear and linear parameters together in a unified framework [125]. The fully nonlinear inversion is to treat linear slip parameters as nonlinear parameters and then use a nonlinear method to solve all of them. For example, Fukuda solved linear fault slips and nonlinear smoothing parameters simultaneously in a Bayesian framework [125]. However, a significant drawback of treating linear parameters as nonlinear parameters relates to computing efficiency since nonlinear inversion requires much more time than linear inversion.

POSTESTIMATION

Geophysical inversion is highly challenging in evaluating the quality of parameter inversion because of the uncertainty of the function model and prior information [126]. Currently, there are many forms of result evaluation. The first type is based on strict statistical inference, which uses EP or parameter interval estimation to quantify parameter estimation errors. The criteria include parameter variance and the CI. This type of result evaluation assumes that the function model and prior information modeling are correct. The second type is nonstatistical testing methods, which have various types and are mainly designed according to the content of concern. They include checkerboard verification, Monte Carlo InSAR observation perturbation simulation, and the model resolution matrix:

- *CI*: When conducting geophysical parameter inversion using Bayesian estimation, the posterior probability density distribution of the parameter can be obtained. Therefore, the CI of the parameter, which is the precision or uncertainty of the parameter, can be obtained naturally while estimating the parameter. This method is relatively objective, so it has become a widely adopted and recognized method. However, it should be noted that Bayesian estimation involves sampling complex posterior probability distributions, and the results may differ depending on the sampling parameter settings. The uncertainty caused by the computational ability cannot be evaluated. Crucially, the parameter posterior probability distribution derived from Bayesian estimation is based on the assumption that the function model and prior information are accurate. However, these assumptions might not hold true in practical scenarios.
- *EP*: For linear estimation processes, the variance of parameters can also be calculated and used to evaluate the quality of estimation. The variance/covariance of a parameter can be directly obtained using variance–covariance propagation. The covariance matrix of the input data of the InSAR deformation field can be estimated using the data from the nondeformed area introduced at the beginning of this section or using the residual after model fitting. Like the CI evaluation method, this method assumes that the function model and prior model are correct. This method is more suitable for accuracy evaluation of parameter estimation after linearization of geophysical nonlinear parameters in relatively simple deformation fields. The main reason is that this situation involves fewer parameters, the function model is approximately accurate, and there is no need to use an artificially assumed prior.
- *Checkerboard validation*: This method is mostly used in earthquake slip distribution inversion. It involves inputting a sliding distribution like a chessboard and comparing the forward InSAR or other observations with the inverted results through consistency comparison [127]. This method was used to validate the resolution of different datasets for slip inversion results [128] and test the effectiveness of new inversion methods [129]. However, such studies conducted only a few simulation tests, and the selected simulated sliding distribution was not consistent with the actual situation, so it cannot fully reflect the real situation from a statistical perspective.
- *Monte Carlo perturbation simulation*: This method determines solution uncertainty by introducing noise perturbations into observations. Wright et al. were among the initial researchers to employ this technique for estimating uncertainty in InSAR inversion [130]. They first estimated the noise structure using observation values from far-field undisturbed areas in InSAR, then generated a large set of spatially correlated InSAR noise based on this structure and incorporated it into the actual InSAR observations. Subsequently, they processed

Authorized licensed use limited to: Shaanxi Normal University. Downloaded on March 14,2024 at 04:23:51 UTC from IEEE Xplore. Restrictions apply.

the dataset with noise interference in InSAR to derive a sample distribution of inverted parameters, indicative of result uncertainty. While widely applied in later studies for assessing uncertainty in the inversion of nonlinear geometric and linear parameters in faults [118], [131], it is crucial to recognize that supplementing InSAR data, which inherently contain noise [132], with simulated noise does not precisely reflect real InSAR data characteristics. Moreover, the resulting uncertainty assessment indicates only parameter sensitivity to perturbations in InSAR results and does not equate to the reliability of these results.

- *Model resolution matrix*: This method uses the diagonal elements of the model resolution matrix of the inversion equation to represent the reliability of the solution. Considering that the inversion process can be represented by a Green function $\boldsymbol{G}$ and its generalized inverse $\mathbf{G}^{-g}$, the relationship between the estimated parameter value $\boldsymbol{m}^{\text{est}}$ and the true value $\boldsymbol{m}^{\text{true}}$ can be expressed as

$$\boldsymbol{m}^{\text{est}} = \mathbf{G}^{-g}\boldsymbol{d} = \mathbf{G}^{-g}\boldsymbol{G}\boldsymbol{m}^{\text{true}} = [\mathbf{G}^{-g}\boldsymbol{G}]\boldsymbol{m}^{\text{true}} = \mathbf{R}\boldsymbol{m}^{\text{true}}. \quad (51)$$

- Here, the matrix $\mathbf{R} = \mathbf{G}^{-g}\boldsymbol{G}$ is the resolution matrix [81], representing the mapping between the true value and the inversion result. If $\mathbf{R}$ is an identity matrix, the estimated value is exactly the same as the true value. The diagonal elements of this matrix represent the degree of approximation between the estimated value and the true value, and the closer to one, the stronger the resolution. In the literature [133], the diagonal elements of the model resolution matrix were used to evaluate the quality of the inversion result. In terms of error theory, the discrepancy between the resolution matrix and the identity matrix represents the bias in the biased estimation error [115]. This discrepancy, to a certain extent, reflects the influence of prior constraints. It is important to note that the generalized inverse, denoted as G^{-g}, can be analytically expressed only within a linear system. Often, inversion processes involve a combination of linear and nonlinear superposition. Furthermore, in cases of linear inversion with the application of nonnegative constraints, it becomes impossible to obtain an analytical expression for G^{-g}. Additionally, it is worth mentioning that resolution primarily measures the bias aspect and does not encompass all the uncertainty features of the inversion solution.

SUMMARY AND FUTURE TRENDS

Over recent decades, the advancement of SAR satellites and related processing methods has positioned InSAR as a standard method for monitoring large-scale ground deformation and deciphering geophysical processes. Statistical inference plays a crucial role in InSAR methods and their applications. This article offered an overview of InSAR deformation measurement and InSAR-constrained geophysical inversion through the lens of statistical inference to facilitate a better understanding of existing methods. It investigated specific statistical inference issues in prevalent PSI, TomoSAR, DSI, and SBAS methods for InSAR processing, along with nonlinear, linear, and mixed-parameter inversion in InSAR-constrained geophysical inversion. Furthermore, the article evaluated current open source code and data resources in the appendix included in the supplementary material. As SAR satellites like the *NASA–Indian Space Research Organization Synthetic Aperture Radar* satellite, *Sentinel 1C*, and various commercial SAR deployments continue to roll out in the coming years, the number of SAR image observations will grow, and the observation frequency will shorten. Comprehensive high-dynamic-range Earth observation will become achievable, spurring further innovations in InSAR geodetic measurement and geophysics. To capitalize on the wealth of SAR data, novel approaches are required in InSAR deformation measurement and InSAR-constrained geophysical parameter estimation. Potential avenues for development include the following:

- *Enabling end-to-end parameter estimation*: As previously discussed, the current process for parameter statistical inference is quite complex, often necessitating multiple steps to transition from observation data to parameters. For example, in MT-InSAR processing, several statistical inference estimation steps are required. These include wrapped phase estimation, unwrapped phase estimation, and deformation estimation. Errors in one step can propagate to the subsequent step, inevitably amplifying estimation errors. A crucial theoretical advancement in future research is to tightly couple this estimation process, potentially allowing for direct geophysical parameter estimation based on SAR raw observations. This would minimize the intermediate preprocessing steps and enable end-to-end parameter estimation. Such an approach would prevent unnecessary parameter estimation errors caused by multistep EP.
- *Leveraging deep neural networks*: This article primarily addressed parameter estimation issues in InSAR and geophysical inversion from an interpretable statistical inference standpoint. Nonetheless, deep learning has demonstrated significant potential in this field. For example, some studies have employed deep learning to aid phase unwrapping [46], [134], [135], identify deformed areas [136], [137], and separate ground deformation signals [132]. However, research in this area remains in its early stages, primarily focused on case studies. Many aspects, such as training samples, network structures, and applicability to different scenarios, remain unexplored. Expanding and developing widely applicable solutions is an essential direction for future research.
- *Enhancing a priori knowledge by integrating multisource datasets*: In many ill-posed estimation problems, the accuracy of prior information modeling significantly impacts parameter estimation. However, many current prior information models are relatively arbitrary,

Authorized licensed use limited to: Shaanxi Normal University. Downloaded on March 14,2024 at 04:23:51 UTC from IEEE Xplore. Restrictions apply.

leading to considerable biases in parameter estimation results and unreliable CI estimation. Future research may focus on fusing multisource data. For example, in geophysical inversion, seismic data and geophysical exploration data can more accurately model the prior probability of parameters. In D-TomoSAR, semantic information can be further integrated. By modeling the prior probability of parameters with external real information constraints, more accurate and reliable parameter estimation can be achieved.

- *Promoting open source InSAR codes*: InSAR geodesy and geophysical inversion play a vital role in sustainable human development and disaster prevention and management. However, compared to popular fields such as computer science and artificial intelligence, research investment and participation in this area remain relatively low. To stimulate growth in the research community, it is crucial to open source advanced processing algorithms. This strategy lowers barriers to entry, encourages wider participation, and consequently drives scientific and technological progress for the betterment of sustainable human development.

ACKNOWLEDGMENT

This work is supported in part by the National Natural Science Foundation of China (Grants 42374018 and 41974006) and Shenzhen Scientific Research and Development Funding Program (Grant RCYX20210706092140076). Bochen Zhang is the corresponding author. This article has supplementary downloadable material available at https://doi.org/10.1109/MGRS.2023.3344159, provided by the authors.

AUTHOR INFORMATION

Chisheng Wang (wangchisheng@szu.edu.cn) received the B.S. degree from Beijing Normal University, Beijing, China, in 2007; the M.S. degree from the Institute of Applied Remote Sensing, Chinese Academy of Science, Beijing, in 2010; and the Ph.D. degree from the Department of Land Surveying and Geo-Informatics, Hong Kong Polytechnic University, Hong Kong, China. He is an associate professor with the Ministry of Natural Resources (MNR) Key Laboratory for Geo-Environmental Monitoring of Great Bay Area and Guangdong Key Laboratory of Urban Informatics, School of Architecture and Urban Planning, Shenzhen University, Shenzhen 518060, China. He worked as a visiting researcher in the department of Earth Observation Science, Faculty of Geo-Information Science and Earth Observation, University of Twente, from 2022 to 2023. He has published more than 40 research articles in high-impact peer-reviewed journals, such as *Remote Sensing of Environment*, *IEEE Transactions on Geoscience and Remote Sensing*, and *ISPRS Journal of Photogrammetry and Remote Sensing*. His research interests focus on developing algorithms for processing interferometric synthetic aperture radar data and applying these algorithms in disaster monitoring and the interpretation of geophysical phenomena.

Ling Chang (ling.chang@utwente.nl) received her M.S. degree in geodesy and survey engineering from Tongji University, Shanghai, China, and her Ph.D. degree from Delft University of Technology (TUDelft), Delft, The Netherlands, in 2010 and 2015. From 2015 to 2018, she worked as a postdoctoral researcher in structural health monitoring of railway infrastructure using satellite radar interferometry in the Department of Structural Engineering, TUDelft. She is currently an associate professor of microwave remote sensing with the Department of Earth Observation Science, Faculty of Geo-Information Science and Earth Observation, University of Twente, 7522 NH Enschede, The Netherlands. Her research interests include statistical hypothesis testing, time series modeling, and change detection using satellite-borne remote sensing technology, particularly interferometric synthetic aperture radar techniques.

Xiang-Sheng Wang (xswang@louisiana.edu) received his B.S. degree from the University of Science and Technology of China, Hefei, China, in 2004 and the Ph.D. degree from the City University of Hong Kong (jointly awarded by the University of Science and Technology of China), Hong Kong, China, in 2009. He is currently an associate professor with the Department of Mathematics, University of Louisiana at Lafayette, Lafayette, LA 70503, USA. His research interests include numerical optimization and approximation theory.

Bochen Zhang (zhangbc@szu.edu.cn) received his B.Eng. degree in geodesy and geomatics from Nanjing University of Technology, Nanjing, China, in 2010 and the M.Sc. degree in geomatics and Ph.D. degree in geodesy and geodynamics from Hong Kong Polytechnic University, Hong Kong, China, in 2012 and 2020, respectively. He is currently an assistant professor with the College of Civil and Transportation Engineering, Shenzhen University, Shenzhen 518060, China. His research interests include developing techniques for spaceborne and terrestrial radar interferometric data processing, with emphasis on geohazards and infrastructure monitoring. He is a Member of IEEE.

Alfred Stein (a.stein@utwente.nl) received his M.Sc. degree in mathematics and information science, with a specialization in applied statistics, from Eindhoven University of Technology, Eindhoven, The Netherlands, and his Ph.D. degree at Wageningen University, Wageningen, The Netherlands. He started his career in the Department of Soil Science and Geology, Wageningen University, leading to a professorship and the chair of mathematical and statistical models in 2000. In 1995, he was appointed a visiting professor at what was then the Institute of ITC, where in 2002 he became a professor in the new Department of Earth Observation Science (EOS), which he has headed for more than 10 years. From 2008 to 2020, he was a member of the faculty board, alternating between portfolios of research and education. He is currently a professor of spatial statistics and image analysis with the

Authorized licensed use limited to: Shaanxi Normal University. Downloaded on March 14,2024 at 04:23:51 UTC from IEEE Xplore. Restrictions apply.

Department of EOS, Faculty of Geo-Information Science and Earth Observation, University of Twente, 7522 NH Enschede, The Netherlands.

REFERENCES

[1] J. R. Elliott, "Earth observation for the assessment of earthquake hazard, risk and disaster management," *Surv. Geophys.*, vol. 41, no. 6, pp. 1323–1354, 2020, doi: 10.1007/s10712-020-09606-4.

[2] J. R. Elliott, R. J. Walters, and T. J. Wright, "The role of space-based observation in understanding and responding to active tectonics and earthquakes," *Nature Commun.*, vol. 7, no. 1, 2016, Art. no. 13844, doi: 10.1038/ncomms13844.

[3] J. Rosen, "Shifting ground," *Science*, vol. 371, no. 6532, pp. 876–880, 2021, doi: 10.1126/science.371.6532.876.

[4] M. Koppes, B. Hallet, E. Rignot, J. Mouginot, J. S. Wellner, and K. Boldt, "Observed latitudinal variations in erosion as a function of glacier dynamics," *Nature*, vol. 526, no. 7571, pp. 100–103, 2015, doi: 10.1038/nature15385.

[5] C. Zhu, C. Wang, B. Zhang, X. Qin, and X. Shan, "Differential Interferometric Synthetic Aperture Radar data for more accurate earthquake catalogs," *Remote Sens. Environ.*, vol. 266, Dec. 2021, Art. no. 112690, doi: 10.1016/j.rse.2021.112690.

[6] S. Staniewicz et al., "InSAR reveals complex surface deformation patterns over an 80,000 km2 oil-producing region in the Permian basin," *Geophys. Res. Lett.*, vol. 47, no. 21, 2020 Art. no. e2020GL090151, doi: 10.1029/2020GL090151.

[7] F. Xue, X. Lv, F. Dou, and Y. Yun, "A review of time-series interferometric SAR techniques: A tutorial for surface deformation analysis," *IEEE Geosci. Remote Sens. Mag.*, vol. 8, no. 1, pp. 22–42, Mar. 2020, doi: 10.1109/MGRS.2019.2956165.

[8] A. Hooper, D. Bekaert, K. Spaans, and M. Arıkan, "Recent advances in SAR interferometry time series analysis for measuring crustal deformation," *Tectonophysics*, vols. 514–517, pp. 1–13, Jan. 2012, doi: 10.1016/j.tecto.2011.10.013.

[9] R. M. J. Amey, A. Hooper, and R. J. Walters, "A Bayesian method for incorporating self-similarity into earthquake slip inversions," *J. Geophys. Res., Solid Earth*, vol. 123, no. 7, pp. 6052–6071, 2018, doi: 10.1029/2017JB015316.

[10] M. Richter, *Inverse Problems: Basics, Theory and Applications in Geophysics*. Cham, Switzerland: Springer Nature, 2021.

[11] G. Casella and R. L. Berger, *Statistical Inference*. Pacific Grove, CA, USA: Duxbury, 2002.

[12] R. Hanssen, *Radar Interferometry: Data Interpretation and Error Analysis*. Dordrecht, The Netherlands: Kluwer, 2001.

[13] C. Wang et al., "A new likelihood function for consistent phase series estimation in distributed scatterer interferometry," *IEEE Trans. Geosci. Remote Sens.*, vol. 60, pp. 1–14, Apr. 2022, doi: 10.1109/TGRS.2022.3170567.

[14] A. M. Guarnieri and S. Tebaldini, "On the exploitation of target statistics for SAR interferometry applications," *IEEE Trans. Geosci. Remote Sens.*, vol. 46, no. 11, pp. 3436–3443, Nov. 2008, doi: 10.1109/TGRS.2008.2001756.

[15] A. Ferretti, A. Fumagalli, F. Novali, C. Prati, and A. Rucci, "A new algorithm for processing interferometric data-stacks: SqueeSAR," *IEEE Trans. Geosci. Remote Sens.*, vol. 49, no. 9, pp. 3460–3470, Sep. 2011, doi: 10.1109/TGRS.2011.2124465.

[16] H. Ansari, F. De Zan, and R. Bamler, "Efficient phase estimation for interferogram stacks," *IEEE Trans. Geosci. Remote Sens.*, vol. 56, no. 7, pp. 4109–4125, Jul. 2018, doi: 10.1109/TGRS.2018.2826045.

[17] P. V. H. Vu, A. Breloy, F. Brigui, Y. Yan, and G. Ginolhac, "Robust phase linking in InSAR," *IEEE Trans. Geosci. Remote Sens.*, vol. 61, no. 1, pp. 1–11, Jun. 2023, doi: 10.1109/TGRS.2023.3289338.

[18] G. Xu, Y. Gao, J. Li, and M. Xing, "InSAR phase denoising: A review of current technologies and future directions," *IEEE Geosci. Remote Sens. Mag.*, vol. 8, no. 2, pp. 64–82, Jun. 2020, doi: 10.1109/MGRS.2019.2955120.

[19] M. S. Seymour and I. G. Cumming, "Maximum likelihood estimation for SAR interferometry," in *Proc. IEEE Int. Geosci. Remote Sens. Symp. (IGARSS)*, 1994, pp. 2272–2275, doi: 10.1109/IGARSS.1994.399711.

[20] J.-S. Lee, "Speckle analysis and smoothing of synthetic aperture radar images," *Comput. Graph. Image Process.*, vol. 17, no. 1, pp. 24–32, 1981, doi: 10.1016/S0146-664X(81)80005-6.

[21] J.-S. Lee, "Refined filtering of image noise using local statistics," *Comput. Graph. Image Process.*, vol. 15, no. 4, pp. 380–389, 1981, doi: 10.1016/S0146-664X(81)80018-4.

[22] R. M. Goldstein and C. L. Werner, "Radar interferogram filtering for geophysical applications," *Geophys. Res. Lett.*, vol. 25, no. 21, pp. 4035–4038, 1998, doi: 10.1029/1998GL900033.

[23] Y. Bian and B. Mercer, "Interferometric SAR phase filtering in the wavelet domain using simultaneous detection and estimation," *IEEE Trans. Geosci. Remote Sens.*, vol. 49, no. 4, pp. 1396–1416, Apr. 2011, doi: 10.1109/TGRS.2010.2076286.

[24] C.-A. Deledalle, L. Denis, F. Tupin, A. Reigber, and M. Jager, "NL-SAR: A unified nonlocal framework for resolution-preserving (Pol)(In)SAR denoising," *IEEE Trans. Geosci. Remote Sens.*, vol. 53, no. 4, pp. 2021–2038, 2015, doi: 10.1109/TGRS.2014.2352555.

[25] M. Çetin et al., "Sparsity-driven synthetic aperture radar imaging: Reconstruction, autofocusing, moving targets, and compressed sensing," *IEEE Signal Process. Mag.*, vol. 31, no. 4, pp. 27–40, Jul. 2014, doi: 10.1109/MSP.2014.2312834.

[26] A. Pepe, Y. Yang, M. Manzo, and R. Lanari, "Improved EMCF-SBAS processing chain based on advanced techniques for the noise-filtering and selection of small baseline multi-look DInSAR interferograms," *IEEE Trans. Geosci. Remote Sens.*, vol. 53, no. 8, pp. 4394–4417, Aug. 2015, doi: 10.1109/TGRS.2015.2396875.

[27] X. Zhu et al., "Deep learning meets SAR: Concepts, models, pitfalls, and perspectives," *IEEE Geosci. Remote Sens. Mag.*, vol. 9, no. 4, pp. 143–172, Dec. 2021, doi: 10.1109/MGRS.2020.3046356.

[28] Y. Wang and X. X. Zhu, "Robust estimators for multipass SAR interferometry," *IEEE Trans. Geosci. Remote Sens.*, vol. 54, no. 2, pp. 968–980, Feb. 2016, doi: 10.1109/TGRS.2015.2471303.

[29] M. Jiang and A. Monti-Guarnieri, "Distributed scatterer interferometry with the refinement of spatiotemporal coherence," *IEEE Trans. Geosci. Remote Sens.*, vol. 58, no. 6, pp. 3977–3987, Jun. 2020, doi: 10.1109/TGRS.2019.2960007.

Authorized licensed use limited to: Shaanxi Normal University. Downloaded on March 14,2024 at 04:23:51 UTC from IEEE Xplore. Restrictions apply.

[30] S. Zwieback and F. J. Meyer, "Reliable InSAR phase history uncertainty estimates," *IEEE Trans. Geosci. Remote Sens.*, vol. 60, pp. 1–9, Jan. 2022, doi: 10.1109/TGRS.2022.3146816.

[31] P. Vu, A. Breloy, F. Brigui, Y. Yan, and G. Ginolhac, "Robust phase linking in InSAR," *IEEE Trans. Geosci. Remote Sens.*, vol. 61, pp. 1–11, Jun. 2023, doi: 10.1109/TGRS.2023.3289338.

[32] P. Vu, F. Brigui, A. Breloy, Y. Yan, and G. Ginolhac, "A new phase linking algorithm for multi-temporal InSAR based on the maximum likelihood estimator," in *Proc. IEEE Int. Geosci. Remote Sens. Symp. (IGARSS)*, 2022, pp. 76–79, doi: 10.1109/IGARSS46834.2022.9884916.

[33] H. Ansari, F. D. Zan, and A. Parizzi, "Study of systematic bias in measuring surface deformation with SAR interferometry," *IEEE Trans. Geosci. Remote Sens.*, vol. 59, no. 2, pp. 1285–1301, Feb. 2021, doi: 10.1109/TGRS.2020.3003421.

[34] F. De Zan, M. Zonno, and P. Lopez-Dekker, "Phase inconsistencies and multiple scattering in SAR interferometry," *IEEE Trans. Geosci. Remote Sens.*, vol. 53, no. 12, pp. 6608–6616, Dec. 2015, doi: 10.1109/TGRS.2015.2444431.

[35] Y. Maghsoudi, A. J. Hooper, T. J. Wright, M. Lazecky, and H. Ansari, "Characterizing and correcting phase biases in short-term, multilooked interferograms," *Remote Sens. Environ.*, vol. 275, Jun. 2022, Art. no. 113022, doi: 10.1016/j.rse.2022.113022.

[36] H. Ansari, F. D. Zan, and R. Bamler, "Sequential estimator: Toward efficient InSAR time series analysis," *IEEE Trans. Geosci. Remote Sens.*, vol. 55, no. 10, pp. 5637–5652, Oct. 2017, doi: 10.1109/TGRS.2017.2711037.

[37] G. Fornaro, S. Verde, D. Reale, and A. Pauciullo, "CAESAR: An approach based on covariance matrix decomposition to improve multibaseline–multitemporal interferometric SAR processing," *IEEE Trans. Geosci. Remote Sens.*, vol. 53, no. 4, pp. 2050–2065, Apr. 2015, doi: 10.1109/TGRS.2014.2352853.

[38] N. Cao, H. Lee, and H. C. Jung, "A phase-decomposition-based PSInSAR processing method," *IEEE Trans. Geosci. Remote Sens.*, vol. 54, no. 2, pp. 1074–1090, Feb. 2016, doi: 10.1109/TGRS.2015.2473818.

[39] D. H. T. Minh and S. Tebaldini, "Interferometric phase linking: Algorithm, application, and perspective," *IEEE Geosci. Remote Sens. Mag.*, vol. 11, no. 3, pp. 46–62, Sep. 2023, doi: 10.1109/MGRS.2023.3300974.

[40] H. Ansari, F. R. Gonzalez, R. Brcic, and F. D. Zan, "Evaluation of ensemble coherence as a measure for stochastic and systematic phase inconsistencies," in *Proc. IEEE Int. Geosci. Remote Sens. Symp. (IGARSS)*, 2019, pp. 417–420, doi: 10.1109/IGARSS.2019.8898691.

[41] B. Kampes, *Radar Interferometry: Persistent Scatterer Technique*. Dordrecht, The Netherlands: Springer, 2014.

[42] A. Ferretti, C. Prati, and F. Rocca, "Permanent scatterers in SAR interferometry," *IEEE Trans. Geosci. Remote Sens.*, vol. 39, no. 1, pp. 8–20, Jan. 2001, doi: 10.1109/36.898661.

[43] A. Hooper and H. A. Zebker, "Phase unwrapping in three dimensions with application to InSAR time series," *J. Opt. Soc. Amer. A*, vol. 24, no. 9, pp. 2737–2747, 2007, doi: 10.1364/JOSAA.24.002737.

[44] H. Yu, H. Lee, T. Yuan, and N. Cao, "A novel method for deformation estimation based on multibaseline InSAR phase unwrapping," *IEEE Trans. Geosci. Remote Sens.*, vol. 56, no. 9, pp. 5231–5243, Sep. 2018, doi: 10.1109/TGRS.2018.2812769.

[45] H. Yu, Y. Lan, Z. Yuan, J. Xu, and H. Lee, "Phase unwrapping in InSAR: A review," *IEEE Geosci. Remote Sens. Mag.*, vol. 7, no. 1, pp. 40–58, Mar. 2019, doi: 10.1109/MGRS.2018.2873644.

[46] L. Zhou, H. Yu, Y. Lan, and m. xing, "Artificial intelligence in interferometric synthetic aperture radar phase unwrapping: A review," *IEEE Geosci. Remote Sens. Mag.*, vol. 9, no. 2, pp. 10–28, Jun. 2021, doi: 10.1109/MGRS.2021.3065811.

[47] G. Fornaro, A. Pauciullo, and F. Serafino, "Deformation monitoring over large areas with multipass differential SAR interferometry: A new approach based on the use of spatial differences," *Int. J. Remote Sens.*, vol. 30, no. 6, pp. 1455–1478, 2009, doi: 10.1080/01431160802459569.

[48] G. Fornaro, A. Pauciullo, and D. Reale, "A null-space method for the phase unwrapping of multitemporal SAR interferometric stacks," *IEEE Trans. Geosci. Remote Sens.*, vol. 49, no. 6, pp. 2323–2334, Jun. 2011, doi: 10.1109/TGRS.2010.2102767.

[49] M. Costantini, S. Falco, F. Malvarosa, F. Minati, F. Trillo, and F. Vecchioli, "Persistent scatterer pair interferometry: Approach and application to COSMO-SkyMed SAR data," *IEEE J. Sel. Topics Appl. Earth Observ. Remote Sens.*, vol. 7, no. 7, pp. 2869–2879, Jul. 2014, doi: 10.1109/JSTARS.2014.2343915.

[50] L. Zhang, Z. Lu, X. Ding, H.-s. Jung, G. Feng, and C.-W. Lee, "Mapping ground surface deformation using temporarily coherent point SAR interferometry: Application to Los Angeles Basin," *Remote Sens. Environ.*, vol. 117, pp. 429–439, Feb. 2012, doi: 10.1016/j.rse.2011.10.020.

[51] J.-C. Lee and M. Shirzaei, "Novel algorithms for pair and pixel selection and atmospheric error correction in multitemporal InSAR," *Remote Sens. Environ.*, vol. 286, Mar. 2023, Art. no. 113447, doi: 10.1016/j.rse.2022.113447.

[52] D. Rife and R. Boorstyn, "Single tone parameter estimation from discrete-time observations," *IEEE Trans. Inf. Theory*, vol. 20, no. 5, pp. 591–598, Sep. 1974, doi: 10.1109/TIT.1974.1055282.

[53] A. Hooper, P. Segall, and H. Zebker, "Persistent scatterer interferometric synthetic aperture radar for crustal deformation analysis, with application to volcan Alcedo, Galapagos," *J. Geophys. Res.*, vol. 112, Jul. 2007, Art. no. B07407, doi: 10.1029/2006JB004763.

[54] A. Hooper, "A multi-temporal InSAR method incorporating both persistent scatterer and small baseline approaches," *Geophys. Res. Lett.*, vol. 35, Aug. 2008, Art. no. L16302, doi: 10.1029/2008GL034654.

[55] P. Berardino, G. Fornaro, R. Lanari, and E. Sansosti, "A new algorithm for surface deformation monitoring based on small baseline differential SAR interferograms," *IEEE Trans. Geosci. Remote Sens.*, vol. 40, no. 11, pp. 2375–2383, Nov. 2002, doi: 10.1109/TGRS.2002.803792.

[56] T. R. Lauknes, H. A. Zebker, and Y. Larsen, "InSAR deformation time series using an L_1-norm small-baseline approach," *IEEE Trans. Geosci. Remote Sens.*, vol. 49, no. 1, pp. 536–546, Jan. 2011, doi: 10.1109/TGRS.2010.2051951.

Authorized licensed use limited to: Shaanxi Normal University. Downloaded on March 14,2024 at 04:23:51 UTC from IEEE Xplore. Restrictions apply.

[57] D. A. Schmidt and R. Bürgmann, "Time-dependent land uplift and subsidence in the Santa Clara valley, California, from a large interferometric synthetic aperture radar data set," *J. Geophys. Res., Solid Earth*, vol. 108, no. B9, p. 2416, 2003, doi: 10.1029/2002JB002267.

[58] P. Ma and H. Lin, "Robust detection of single and double persistent scatterers in urban built environments," *IEEE Trans. Geosci. Remote Sens.*, vol. 54, no. 4, pp. 2124–2139, Apr. 2016, doi: 10.1109/TGRS.2015.2496193.

[59] F. J. Van Leijen, "Persistent scatterer interferometry based on geodetic estimation theory," Ph.D. dissertation, Delft Univ. Technol., Delft, The Netherlands, 2014.

[60] Z. Li et al., "Time-series InSAR ground deformation monitoring: Atmospheric delay modeling and estimating," *Earth-Sci. Rev.*, vol. 192, pp. 258–284, May 2019, doi: 10.1016/j.earscirev.2019.03.008.

[61] S. Xiong, C. Wang, X. Qin, B. Zhang, and Q. Li, "Time-series analysis on persistent scatter-interferometric synthetic aperture radar (PS-InSAR) derived displacements of the Hong Kong–Zhuhai–Macao bridge (HZMB) from Sentinel-1A observations," *Remote Sens.*, vol. 13, no. 4, 2021, Art. no. 546, doi: 10.3390/rs13040546.

[62] L. Chang, "Monitoring civil infrastructure using satellite radar interferometry," Ph.D. dissertation, Delft Univ. Technol., Delft, The Netherlands, 2015.

[63] D. Just and R. Bamler, "Phase statistics of interferograms with applications to synthetic aperture radar," *Appl. Opt.*, vol. 33, no. 20, pp. 4361–4368, 1994, doi: 10.1364/AO.33.004361.

[64] P. J. Teunissen and A. Amiri-Simkooei, "Least-squares variance component estimation," *J. Geodesy*, vol. 82, pp. 65–82, Feb. 2008, doi: 10.1007/s00190-007-0157-x.

[65] X. Wan, Z. Li, E. Chen, L. Zhao, W. Zhang, and K. Xu, "Forest aboveground biomass estimation using multi-features extracted by fitting vertical backscattered power profile of tomographic SAR," *Remote Sens.*, vol. 13, no. 2, 2021, Art. no. 186, doi: 10.3390/rs13020186.

[66] M. Pardini, V. Cazcarra-Bes, and K. P. Papathanassiou, "Tomo-SAR mapping of 3D forest structure: Contributions of L-band configurations," *Remote Sens.*, vol. 13, no. 12, 2021, Art. no, 2255, doi: 10.3390/rs13122255.

[67] M. Schmitt, M. Shahzad, and X. X. Zhu, "Reconstruction of individual trees from multi-aspect TomoSAR data," *Remote Sens. Environ.*, vol. 165, pp. 175–185, Aug. 2015, doi: 10.1016/j.rse.2015.05.012.

[68] W. Yuanyuan, Z. Xiao Xiang, and R. Bamler, "An efficient tomographic inversion approach for urban mapping using meter resolution SAR image stacks," *IEEE Geosci. Remote Sens. Lett.*, vol. 11, no. 7, pp. 1250–1254, Jul. 2014, doi: 10.1109/LGRS.2013.2290833.

[69] X. X. Zhu, N. Ge, and M. Shahzad, "Joint sparsity in SAR tomography for urban mapping," *IEEE J. Sel. Topics Signal Process.*, vol. 9, no. 8, pp. 1498–1509, Dec. 2015, doi: 10.1109/JSTSP.2015.2469646.

[70] P. Ma, "Robust detection of single and double persistent scatterers in urban built environments: The Tomo-PSInSAR method," Ph.D. dissertation, The Chinese Univ. of Hong Kong, Hong Kong, China, 2016.

[71] X. X. Zhu, Y. Wang, S. Gernhardt, and R. Bamler, "TomoGENESIS: DLR's tomographic SAR processing system," in *Proc. Joint Urban Remote Sens. Event*, 2013, pp. 159–162, doi: 10.1109/JURSE.2013.6550690.

[72] G. Fornaro, F. Lombardini, and F. Serafino, "Three-dimensional multipass SAR focusing: experiments with long-term spaceborne data," *IEEE Trans. Geosci. Remote Sens.*, vol. 43, no. 4, pp. 702–714, Apr. 2005, doi: 10.1109/TGRS.2005.843567.

[73] G. Fornaro, D. Reale, and F. Serafino, "Four-dimensional SAR imaging for height estimation and monitoring of single and double scatterers," *IEEE Trans. Geosci. Remote Sens.*, vol. 47, no. 1, pp. 224–237, Jan. 2009, doi: 10.1109/TGRS.2008.2000837.

[74] X. X. Zhu and R. Bamler, "Demonstration of super-resolution for tomographic SAR imaging in urban environment," *IEEE Trans. Geosci. Remote Sens.*, vol. 50, no. 8, pp. 3150–3157, Aug. 2012, doi: 10.1109/TGRS.2011.2177843.

[75] I. Daubechies, M. Defrise, and C. De Mol, "An iterative thresholding algorithm for linear inverse problems with a sparsity constraint," *Commun. Pure Appl. Math.*, vol. 57, no. 11, pp. 1413–1457, Aug. 2004, doi: 10.1002/cpa.20042.

[76] K. Qian, Y. Wang, Y. Shi, and X. X. Zhu, "γ-Net: Superresolving SAR tomographic inversion via deep learning," *IEEE Trans. Geosci. Remote Sens.*, vol. 60, pp. 1–16, Apr. 2022, doi: 10.1109/TGRS.2022.3164193.

[77] A. Pauciullo, D. Reale, A. De Maio, and G. Fornaro, "Detection of double scatterers in SAR tomography," *IEEE Trans. Geosci. Remote Sens.*, vol. 50, no. 9, pp. 3567–3586, Sep. 2012, doi: 10.1109/TGRS.2012.2183002.

[78] A. De Maio, G. Fornaro, and A. Pauciullo, "Detection of single scatterers in multidimensional SAR imaging," *IEEE Trans. Geosci. Remote Sens.*, vol. 47, no. 7, pp. 2284–2297, Jul. 2009, doi: 10.1109/TGRS.2008.2011632.

[79] X. X. Zhu and R. Bamler, "Very high resolution spaceborne SAR tomography in urban environment," *IEEE Trans. Geosci. Remote Sens.*, vol. 48, no. 12, pp. 4296–4308, Dec. 2010, doi: 10.1109/TGRS.2010.2050487.

[80] F. Lombardini and F. Gini, "Model order selection in multibaseline interferometric radar systems," *EURASIP J. Adv. Signal Process.*, vol. 2005, no. 20, pp. 1–14, 2005, doi: 10.1155/ASP.2005.3206.

[81] W. Menke, *Geophysical Data Analysis: Discrete Inverse Theory*. San Diego, CA, USA: Academic, 2018.

[82] R. Sato, "Crustal deformation due to dislocation in a multilayered medium," *J. Phys. Earth*, vol. 19, no. 1, pp. 31–46, 1971, doi: 10.4294/jpe1952.19.31.

[83] R. Sato and M. Matsu'ura, "Static deformation due to the fault spreading over several layers in a multi-layered medium part I: Displacement," *J. Phys. Earth*, vol. 21, no. 3, pp. 227–249, 1973, doi: 10.4294/jpe1952.21.227.

[84] D. B. Jovanovich, M. I. Husseini, and M. A. Chinnery, "Elastic dislocations in a layered half-space-1. Basic theory and numerical methods," *Geophys. J. Roy. Astron. Soc.*, vol. 39, no. 2, pp. 205–217, 1974, doi: 10.1111/j.1365-246X.1974.tb05451.x.

Authorized licensed use limited to: Shaanxi Normal University. Downloaded on March 14,2024 at 04:23:51 UTC from IEEE Xplore. Restrictions apply.

[85] S. Zhao, R. Muller, Y. Takahashi, and Y. Kaneda, "3D finite element modelling of deformation and stress associated with faulting: effect of inhomogeneous crustal structures," *Geophys. J. Int.*, vol. 157, no. 2, pp. 629–644, 2004, doi: 10.1111/j.1365-246X.2004.02200.x.

[86] T. Masterlark and K. L. H. Hughes, "Next generation of deformation models for the 2004 M9 Sumatra-Andaman earthquake," *Geophys. Res. Lett.*, vol. 35, no. 19, 2008. Art. no. 19310, doi: 10.1029/2008GL035198.

[87] C. Wang, X. Shan, C. Wang, X. Ding, G. Zhang, and T. Masterlark, "Using finite element and Okada models to invert coseismic slip of the 2008 Mw 7.2 Yutian earthquake, China, from InSAR data," *J. Seismol.*, vol. 17, no. 2, pp. 347–360, 2013, doi: 10.1007/s10950-012-9324-5.

[88] J.-P. Avouac, "From geodetic imaging of seismic and aseismic fault slip to dynamic modeling of the seismic cycle," *Annu. Rev. Earth Planet. Sci.*, vol. 43, no. 1, pp. 233–271, 2015, doi: 10.1146/annurev-earth-060614-105302.

[89] Y. Okada, "Surface deformation due to shear and tensile faults in a half-space," *Bull. Seismol. Soc. Amer.*, vol. 75, no. 4, pp. 1135–1154, 1985, doi: 10.1785/BSSA0750041135.

[90] J. Fukuda and K. M. Johnson, "Bayesian inversion for a stress-driven model of afterslip and viscoelastic relaxation: Method and application to postseismic deformation following the 2011 MW 9.0 Tohoku-oki earthquake," *J. Geophys. Res., Solid Earth*, vol. 126, no. 5, 2021, Art. no. e2020JB021620, doi: 10.1029/2020JB021620.

[91] S. Barbot and Y. Fialko, "A unified continuum representation of post-seismic relaxation mechanisms: semi-analytic models of afterslip, poroelastic rebound and viscoelastic flow," *Geophys. J. Int.*, vol. 182, no. 3, pp. 1124–1140, 2010, doi: 10.1111/j.1365-246X.2010.04678.x.

[92] N. C. Taylor, J. H. Johnson, and R. A. Herd, "Making the most of the Mogi model: Size matters," *J. Volcanol. Geothermal Res.*, vol. 419, 2021, Art. no. 107380, doi: 10.1016/j.jvolgeores.2021.107380.

[93] M. Nikkhoo, T. R. Walter, P. R. Lundgren, and P. Prats-Iraola, "Compound dislocation models (CDMs) for volcano deformation analyses," *Geophys. J. Int.*, vol. 208, no. 2, pp. 877–894, 2016, doi: 10.1093/gji/ggw427.

[94] X. M. Yang, P. M. Davis, and J. H. Dieterich, "Deformation from inflation of a dipping finite prolate spheroid in an elastic half-space as a model for volcanic stressing," *J. Geophys. Res., Solid Earth*, vol. 93, no. B5, pp. 4249–4257, 1988, doi: 10.1029/JB093iB05p04249.

[95] Y. Fialko, D. Sandwell, D. Agnew, M. Simons, P. Shearer, and B. Minster, "Deformation on nearby faults induced by the 1999 Hector Mine earthquake," *Science*, vol. 297, no. 5588, pp. 1858–1862, 2002. doi: 10.1126/science.1074671.

[96] J. Ruch, T. Wang, W. Xu, M. Hensch, and S. Jónsson, "Oblique rift opening revealed by reoccurring magma injection in central Iceland," *Nature Commun.*, vol. 7, no. 1, 2016, Art. no. 12352, doi: 10.1038/ncomms12352.

[97] W. Xu, J. Ruch, and S. Jónsson, "Birth of two volcanic islands in the southern Red Sea," *Nature Commun.*, vol. 6, no. 1, 2015, Art. no. 7104, doi: 10.1038/ncomms8104.

[98] G. Currenti, A. Bonaccorso, C. Del Negro, D. Scandura, and E. Boschi, "Elasto-plastic modeling of volcano ground deformation," *Earth Planet. Sci. Lett.*, vol. 296, nos. 3–4, pp. 311–318, 2010, doi: 10.1016/j.epsl.2010.05.013.

[99] J. Hickey, J. Gottsmann, H. Nakamichi, and M. Iguchi, "Thermomechanical controls on magma supply and volcanic deformation: application to Aira caldera, Japan," *Scientific Rep.*, vol. 6, no. 1, 2016, Art. no. 32691, doi: 10.1038/srep32691.

[100] E. Trasatti, C. Giunchi, and N. P. Agostinetti, "Numerical inversion of deformation caused by pressure sources: application to Mount Etna (Italy)," *Geophys. J. Int.*, vol. 172, no. 2, pp. 873–884, 2008, doi: 10.1111/j.1365-246X.2007.03677.x.

[101] A. Bonaccorso, S. Cianetti, C. Giunchi, E. Trasatti, M. Bonafede, and E. Boschi, "Analytical and 3-D numerical modelling of Mt. Etna (Italy) volcano inflation," *Geophys. J. Int.*, vol. 163, no. 2, pp. 852–862, 2005, doi: 10.1111/j.1365-246X.2005.02777.x.

[102] J. Chen, R. Knight, H. A. Zebker, and W. A. Schreüder, "Confined aquifer head measurements and storage properties in the San Luis Valley, Colorado, from spaceborne InSAR observations," *Water Resour. Res.*, vol. 52, no. 5, pp. 3623–3636, 2016, doi: 10.1002/2015WR018466.

[103] E. Chaussard, P. Milillo, R. Bürgmann, D. Perissin, E. J. Fielding, and B. Baker, "Remote sensing of ground deformation for monitoring groundwater management practices: Application to the Santa Clara Valley during the 2012–2015 California drought," *J. Geophys. Res., Solid Earth*, vol. 122, no. 10, pp. 8566–8582, 2017, doi: 10.1002/2017JB014676.

[104] H. Fan, T. Li, Y. Gao, K. Deng, and H. Wu, "Characteristics inversion of underground goaf based on InSAR techniques and PIM," *Int. J. Appl. Earth Observ. Geoinf.*, vol. 103, Dec. 2021, Art. no. 102526, doi: 10.1016/j.jag.2021.102526.

[105] A. Gray, N. Short, K. Mattar, and K. Jezek, "Velocities and flux of the Filchner Ice Shelf and its tributaries determined from speckle tracking interferometry," *Can. J. Remote Sens.*, vol. 27, no. 3, pp. 193–206, 2001, doi: 10.1080/07038992.2001.10854936.

[106] J. Li et al., "Deriving a time series of 3D glacier motion to investigate interactions of a large mountain glacial system with its glacial lake: Use of Synthetic Aperture Radar Pixel Offset-Small Baseline Subset technique," *J. Hydrol.*, vol. 559, pp. 596–608, Apr. 2018, doi: 10.1016/j.jhydrol.2018.02.067.

[107] H. Sudhaus, and J. Sigurjón, "Improved source modelling through combined use of InSAR and GPS under consideration of correlated data errors: Application to the June 2000 Kleifarvatn earthquake, Iceland," *Geophys. J. Int.*, vol. 176, no. 2, pp. 389–404, 2009, doi: 10.1111/j.1365-246X.2008.03989.x.

[108] J.-P. Chiles and P. Delfiner, *Geostatistics: Modeling Spatial Uncertainty*. Hoboken, NJ, USA: Wiley, 2012.

[109] J. Fukuda and K. M. Johnson, "Mixed linear-on-linear inversion of crustal deformation data: Bayesian inference of model, weighting and regularization parameters," *Geophys. J. Int.*, vol. 181, no. 3, pp. 1441–1458, 2010, doi: 10.1111/j.1365-246X.2010.04564.x.

[110] R. C. Aster, C. H. Thurber, and B. Borchers, *Parameter Estimation and inverse Problems*. Amsterdam, The Netherlands: Elsevier, 2013.

Authorized licensed use limited to: Shaanxi Normal University. Downloaded on March 14,2024 at 04:23:51 UTC from IEEE Xplore. Restrictions apply.

[111] A. Tarantola, *Inverse Problem Theory: Methods for Data Fitting and Model Parameter Estimation*. Philadelphia, PA, USA: SIAM, 2005.

[112] R. Hanssen, S. Verhagen, and S. S. Esfahany, "Observation theory: Estimating the unknown," edX, Cambridge, MA, USA, 2022. [Online]. Available: https://learning.edx.org/course/course-v1:DelftX+OT.1x+2T2021/home

[113] M. S. Zhdanov, *Geophysical Inverse Theory and Regularization Problems*. New York, NY, USA: Elsevier, 2002.

[114] M. Bagnardi, and A. Hooper, "Inversion of surface deformation data for rapid estimates of source parameters and uncertainties: A Bayesian approach," *Geochem., Geophys., Geosyst.*, vol. 19, no. 7, pp. 2194–2211, 2018, doi: 10.1029/2018GC007585.

[115] C. Wang et al., "Adaptive regularization of earthquake slip distribution inversion," *Tectonophysics*, vol. 675, pp. 181–195, Apr. 2016, doi: 10.1016/j.tecto.2016.03.018.

[116] L. Yi et al., "Joint inversion of GPS, InSAR and teleseismic data sets for the rupture process of the 2015 Gorkha, Nepal, earthquake using a generalized ABIC method," *J. Asian Earth Sci.*, vol. 148, pp. 121–130, Oct. 2017, doi: 10.1016/j.jseaes.2017.08.029.

[117] Y. Fukahata and T. J. Wright, "A non-linear geodetic data inversion using ABIC for slip distribution on a fault with an unknown dip angle," *Geophys. J. Int.*, vol. 173, no. 2, pp. 353–364, 2008, doi: 10.1111/j.1365-246X.2007.03713.x.

[118] T. J. Wright, Z. Lu, and C. Wicks, "Constraining the slip distribution and fault geometry of the Mw 7.9, 3 November 2002, Denali fault earthquake with interferometric synthetic aperture radar and global positioning system data," *Bull. Seismol. Soc. Amer.*, vol. 94, no. 6B, pp. S175–S189, 2004, doi: 10.1785/0120040623.

[119] T. Arnaddottir and P. Segall, "The 1989 Loma Prieta earthquake imaged from inversion of geodetic data," *J. Geophys. Res., Solid Earth*, vol. 99, no. B11, pp. 21,835–21,855, 1994, doi: 10.1029/94JB01256.

[120] S. Jonsson, H. Zebker, P. Segall, and F. Amelung, "Fault slip distribution of the 1999 Mw 7.1 Hector Mine, California, earthquake, estimated from satellite radar and GPS measurements," *Bull. Seismol. Soc. Amer.*, vol. 92, no. 4, pp. 1377–1389, 2002, doi: 10.1785/0120000922.

[121] D. Schmidt and R. Burgmann, "InSAR constraints on the source parameters of the 2001 Bhuj earthquake," *Geophys. Res. Lett.*, vol. 33, no. 2, 2006, Art. no. L02315, doi: 10.1029/2005GL025109.

[122] M. Talebian et al., "The 2003 Bam (Iran) earthquake: Rupture of a blind strike-slip fault," *Geophys. Res. Lett.*, vol. 31, no. 11, 2004, Art. no. L11611, doi: 10.1029/2004GL020058.

[123] Y. Fialko, "Probing the mechanical properties of seismically active crust with space geodesy: Study of the co-seismic deformation due to the 1992 Mw7. 3 Landers (southern California) earthquake," *J. Geophys. Res., Solid Earth*, vol. 109, no. B3, 2004, Art. no. B03307, doi: 10.1029/2003JB002756.

[124] Z. K. Shen et al., "Slip maxima at fault junctions and rupturing of barriers during the 2008 Wenchuan earthquake," *Nature Geosci.*, vol. 2, no. 10, pp. 718–724, 2009, doi: 10.1038/ngeo636.

[125] J. Fukuda and K. M. Johnson, "A fully Bayesian inversion for spatial distribution of fault slip with objective smoothing," *Bull. Seismol. Soc. Amer.*, vol. 98, no. 3, pp. 1128–1146, 2008, doi: 10.1785/0120070194.

[126] I. A. Beresnev, "Uncertainties in finite-fault slip inversions: to what extent to believe? (A critical review)," *Bull. Seismol. Soc. Amer.*, vol. 93, no. 6, pp. 2445–2458, 2003, doi: 10.1785/0120020225.

[127] C. Wang, X. Ding, X. Shan, L. Zhang, and M. Jiang, "Slip distribution of the 2011 Tohoku earthquake derived from joint inversion of GPS, InSAR and seafloor GPS/acoustic measurements," *J. Asian Earth Sci.*, vol. 57, pp. 128–136, Sep. 2012, doi: 10.1016/j.jseaes.2012.06.019.

[128] B. Delouis, D. Giardini, P. Lundgren, and J. Salichon, "Joint inversion of InSAR, GPS, teleseismic, and strong-motion data for the spatial and temporal distribution of earthquake slip: Application to the 1999 Izmit mainshock," *Bull. Seismol. Soc. Amer.*, vol. 92, no. 1, pp. 278–299, 2002, doi: 10.1785/0120000806.

[129] J. Sun, K. M. Johnson, Z. Cao, Z. Shen, R. Burgmann, and X. Xu, "Mechanical constraints on inversion of coseismic geodetic data for fault slip and geometry: Example from InSAR observation of the 6 October 2008 Mw 6.3 Dangxiong-Yangyi (Tibet) earthquake," *J. Geophys. Res., Solid Earth*, vol. 116, Jan. 2011, Art. no. B01406, doi: 10.1029/2010JB007849.

[130] T. Wright, P. Clarke, and G. Funning, "Realistic error modelling for InSAR: Determination of uncertainties in earthquake slip distributions," in *Proc. AGU Fall Meeting*, 2002, pp. G61B–0998.

[131] J. Elliott, R. Walters, P. England, J. Jackson, Z. Li, and B. Parsons, "Extension on the Tibetan plateau: recent normal faulting measured by InSAR and body wave seismology," *Geophys. J. Int.*, vol. 183, no. 2, pp. 503–535, 2010, doi: 10.1111/j.1365-246X.2010.04754.x.

[132] B. Rouet-Leduc, R. Jolivet, M. Dalaison, P. A. Johnson, and C. Hulbert, "Autonomous extraction of millimeter-scale deformation in InSAR time series using deep learning," *Nature Commun.*, vol. 12, no. 1, 2021, Art. no. 6480, doi: 10.1038/s41467-021-26254-3.

[133] M. T. Page, S. Custódio, R. J. Archuleta, and J. Carlson, "Constraining earthquake source inversions with GPS data: 1. Resolution-based removal of artifacts," *J. Geophys. Res., Solid Earth*, vol. 114, 2009, Art. no. B01314, doi: 10.1029/2007JB005449.

[134] Z. Wu, T. Wang, Y. Wang, R. Wang, and D. Ge, "Deep-learning-based phase discontinuity prediction for 2-D phase unwrapping of SAR interferograms," *IEEE Trans. Geosci. Remote Sens.*, vol. 60, pp. 1–16, 2022, doi: 10.1109/TGRS.2021.3121906.

[135] L. Zhou, H. Yu, V. Pascazio, and M. Xing, "PU-GAN: a one-step 2-D InSAR phase unwrapping based on conditional generative adversarial network," *IEEE Trans. Geosci. Remote Sens.*, vol. 60, pp. 1–10, 2022, doi: 10.1109/TGRS.2022.3145342.

[136] C. P. Schwegmann, W. Kleynhans, J. Engelbrecht, L. W. Mdakane, and R. G. V. Meyer, "Subsidence feature discrimination using deep convolutional neural networks in synthetic aperture radar imagery," in *Proc. IEEE Int. Geosci. Remote Sens. Symp. (IGARSS)*, 2017, pp. 4626–4629, doi: 10.1109/IGARSS.2017.8128031.

[137] P. Milillo, G. Sacco, D. Di Martire, and H. Hua, "Neural network pattern recognition experiments toward a fully automatic detection of anomalies in InSAR time series of surface deformation," *Frontiers Earth Sci.*, vol. 9, Feb. 2022, Art. no. 728643, doi: 10.3389/feart.2021.728643.

GRS

Authorized licensed use limited to: Shaanxi Normal University. Downloaded on March 14,2024 at 04:23:51 UTC from IEEE Xplore. Restrictions apply.